

1 **Quantification of the dust optical depth across spatiotemporal scales with the
2 MIDAS global dataset (2003-2017)**

3

4 Antonis Gkikas¹, Emmanouil Proestakis¹, Vassilis Amiridis¹, Stelios Kazadzis^{2,3}, Enza Di Tomaso⁴,
5 Eleni Marinou^{1,5}, Nikos Hatzianastassiou⁶, Jasper F. Kok⁷ and Carlos Pérez García-Pando^{4,8}

6

7 ¹Institute for Astronomy, Astrophysics, Space Applications and Remote Sensing, National Observatory of Athens,
8 Athens, 15236, Greece

9 ²Physikalisch-Meteorologisches Observatorium Davos, World Radiation Center, Switzerland

10 ³Institute of Environmental Research and Sustainable Development, National Observatory of Athens, Greece

11 ⁴Barcelona Supercomputing Center, Barcelona, Spain

12 ⁵Deutsches Zentrum für Luft- und Raumfahrt (DLR), Institut für Physik der Atmosphäre, Oberpfaffenhofen, Germany

13 ⁶Laboratory of Meteorology, Department of Physics, University of Ioannina, Ioannina, Greece

14 ⁷Department of Atmospheric and Oceanic Sciences, University of California, Los Angeles, CA 90095, USA

15 ⁸ICREA, Catalan Institution for Research and Advanced Studies, Barcelona, Spain

16

17 Corresponding author: Antonis Gkikas (agkikas@noa.gr)

18

19 **Abstract**

20 Quantifying the dust optical depth (DOD) and its uncertainty across spatiotemporal scales is key to
21 understanding and constraining the dust cycle and its interactions with the Earth System. This study
22 quantifies the DOD along with its monthly and year-to-year variability between 2003 and 2017 at
23 global and regional levels based on the MIDAS (ModIs Dust AeroSol) dataset, which combines
24 MODIS-Aqua retrievals and MERRA-2 reanalysis products. We also describe the annual and
25 seasonal geographical distributions of DOD across the main dust source regions and transport
26 pathways. MIDAS provides columnar mid-visible (550 nm) DOD at fine spatial resolution ($0.1^\circ \times$
27 0.1°), expanding the current observational capabilities for monitoring the highly variable
28 spatiotemporal features of the dust burden. We obtain a global DOD of 0.032 ± 0.003 – approximately
29 a quarter ($23.4\% \pm 2.4\%$) of the global AOD – with about one order of magnitude more DOD in the
30 northern hemisphere (0.056 ± 0.004 ; $31.8\% \pm 2.7\%$) than in the southern hemisphere (0.008 ± 0.001 ;
31 $8.2\% \pm 1.1\%$) and about 3.5 times more DOD over land (0.070 ± 0.005) than over ocean ($0.019 \pm$
32 0.002). The northern hemisphere monthly DOD is highly correlated with the corresponding monthly
33 AOD ($R^2=0.94$) and contributes 20% to 48% of it, both indicating a dominant dust contribution. In
34 contrast, the contribution of dust to the monthly AOD does not exceed 17% in the southern
35 hemisphere, although the uncertainty in this region is larger. Among the major dust sources of the
36 planet, the maximum DODs (~1.2) are recorded in the Bodélé Depression of the northern Lake Chad
37

38 Basin, whereas moderate-to-high intensities are encountered in the Western Sahara (boreal summer),
39 along the eastern parts of the Middle East (boreal summer) and in the Taklamakan Desert (spring).
40 Over oceans, major long-range dust transport is observed primarily along the Tropical Atlantic
41 (intensified during boreal summer) and secondarily in the North Pacific (intensified during boreal
42 spring). Our calculated global and regional averages and associated uncertainties are consistent with
43 some but not all recent observationally based studies. Our work provides a simple, yet flexible method
44 to estimate consistent uncertainties across spatiotemporal scales, which will enhance the use of the
45 MIDAS dataset in a variety of future studies.

46

47 **1. Introduction**

48 Mineral dust particles are emitted throughout the year across the arid and semi-arid regions of the
49 planet, when winds exceed a threshold velocity mainly determined by soil texture, soil moisture, and
50 surface roughness. While dust aerosols have mainly a natural origin, the contribution of
51 anthropogenic land use is estimated to be between 10% and 25 % (Tegen et al. 2004; Stanelle et al.,
52 2014; Ginoux et al., 2012). Dust is mobilized by microscale to synoptic scale phenomena, from dust
53 devils developed under strong surface heating (Koch and Renno, 2005), to “haboobs” formed by
54 intense cold-pool downdrafts related to deep moist convection (Knippertz et al., 2007), to synoptic
55 patterns associated with intensified pressure gradients (Klose et al., 2010) and low-level jets (LLJ;
56 Fiedler et al., 2013). Meteorology also plays a key role in the dust transport over maritime areas taking
57 place mainly across the Tropical Atlantic Ocean (Prospero and Mayol-Bracero, 2013; Yu et al., 2015),
58 the northern Pacific Ocean (Husar et al., 2001), the Mediterranean (Flaounas et al., 2015; Gkikas et
59 al., 2015), the Arabian Sea (Ramaswamy et al., 2017) and the southern Atlantic Ocean (Gasso and
60 Stein, 2007). Dust perturbs the radiation budget through direct (Sokolik and Toon, 1996), semi-direct
61 (Huang et al., 2006) and indirect (Haywood and Bucher, 2000) processes, leading to impacts upon
62 weather (Pérez et al., 2006; Gkikas et al., 2018; Gkikas et al., 2019) and climate (Lambert et al., 2013;
63 Nabat et al., 2015). Upon deposition, nutrient-rich dust particles can increase the productivity of
64 oceanic waters (Jickells et al., 2005) and terrestrial ecosystems (Okin et al., 2004) and perturb the
65 carbon cycle (Jickells et al., 2014). Dust has been associated with epidemics of meningococcal
66 meningitis in the African Sahel (Pérez García-Pando et al., 2014a, b) and with air quality degradation
67 in urban areas (Kanakidou et al., 2011) causing respiratory (Kanatani et al., 2010) and cardiovascular
68 (Du et al., 2016) disease when the population is exposed to high dust concentrations (Querol et al.,
69 2019). Other socio-economic sectors can be regionally affected by dust storms (Middleton, 2017),
70 including transportation (Weinzierl et al., 2012), agriculture (Stefanski and Sivakumar, 2009) and
71 solar energy production (Kosmopoulos et al., 2018).

72 Satellite measurements and numerical simulations have repeatedly shown the remarkable contrast
73 in dust load between the two hemispheres. The substantially higher dust load in the N. Hemisphere
74 is associated to the wider deserts extending across the so-called “dust belt” (Prospero et al., 2002;
75 Ginoux et al., 2012) in contrast to the smaller sources in Australia, South Africa and South America.
76 At global scale, most of the entrained dust loads in the atmosphere originate from tropical and sub-
77 tropical arid regions; yet, it is estimated that up to 5% of the global dust budget consists of particles
78 emitted from high-latitude sources (Bullard and Austin, 2011; Bullard et al., 2016). Given the key
79 role of dust aerosols in the Earth system it is imperative to monitor and understand the global dust
80 cycle along with its multi-scale spatiotemporal variability over long time periods and fine spatial
81 resolution. This task can be fulfilled to a certain degree using contemporary satellite instruments
82 providing accurate retrievals and global coverage over extended time periods. With this approach,
83 one of the key challenges is to discriminate dust from other aerosols. Several studies have combined
84 AOD and aerosol index (AI) (e.g., Middleton and Goudie, 2001; Prospero et al., 2002) or AOD, single
85 scattering albedo (SSA) and Ångström exponent (AE) (Ginoux et al., 2012) to identify the most active
86 dust sources worldwide. Other studies have focused on the dust load and its variability in specific
87 regions such as the Atlantic Ocean and the Arabian Sea (Peyridieu et al., 2013), the Sistan basin
88 (Rashki et al., 2015), the Mediterranean (Gkikas et al., 2016), Europe and North Africa (Marinou et
89 al., 2017) and east Asia (Proestakis et al., 2018), among others. Liu et al. (2008) described the three-
90 dimensional structure of dust aerosols at global scale based on CALIOP vertically resolved retrievals
91 acquired during the first operational year of the CALIPSO satellite mission. A more advanced
92 approach has been introduced by Amiridis et al. (2013) and Marinou et al. (2017), who applied a
93 more realistic lidar ratio for the Saharan dust and a series of quality filters on the CALIOP vertical
94 profiles, in order to provide information about the vertical structure of dust layers at global scale and
95 coarse resolution in the LIVAS dataset (Amiridis et al., 2015). Ridley et al. (2016) quantified the
96 global average DOD and its uncertainty for the period 2004-2008 based on AOD retrievals from
97 passive spaceborne sensors (MODIS, MISR), ground-based (AERONET) and shipborne (MAN)
98 measurements from sun-photometers, and numerical simulations. Voss and Evan (2020) provided a
99 long-term DOD climatology over the Tropics and mid-latitudes at a coarse spatial resolution ($1^\circ \times$
100 1°) based on MODIS and AVHRR observations, where DOD was estimated based on AOD, SSA and
101 AE over land following Ginoux et al. (2012) and AOD, fine and coarse AOD (AERONET) and
102 MERRA-2 winds over ocean. Based on vertically-resolved CALIOP retrievals and columnar MODIS
103 optical properties, Song et al. (2021) provided a long-term 4D global dust optical depth dataset,
104 excluding the polar regions, over the period 2007 – 2019. In their approach, they took advantage of
105 spaceborne observations that can be used for the discrimination/identification of dust aerosols
106 characterized by their aspherical shape, coarse size and absorption.

107 Our study provides a global and regional quantification and description of the DOD based on the
108 new ModIs Dust AeroSol (MIDAS) dataset (Gkikas et al., 2021). The powerful and innovative
109 elements of the MIDAS DOD dataset are the: (i) daily availability and fine spatial resolution ($0.1^\circ \times$
110 0.1°), (ii) full global coverage including the sources and downwind areas (both over land and sea),
111 (iii) 15-year temporal range (2003 – 2017) using the most updated MODIS data collection, (iv) grid-
112 cell level uncertainty quantification. In this contribution, we first describe the annual and seasonal
113 geographical distribution of DOD across the main dust source regions and transport pathways
114 (Section 4.1). We then quantify the average DOD and its monthly and year-to-year variability at
115 global, hemispherical and regional levels, along with its fractional contribution to the AOD (Section
116 4.2). We summarize the main findings in Section 5.

117 **2. ModIs Dust AeroSol (MIDAS) dataset**

118 Our study is based on the MIDAS global fine resolution dataset described in detail in Gkikas et
119 al. (2021). We analyse the DOD at 550 nm at $0.1^\circ \times 0.1^\circ$ spatial resolution between 2003 to 2017.
120 The MIDAS DOD results from the combination of the quality-filtered MODIS aerosol optical depth
121 (AOD, Collection 6.1, Level 2; Levy et al., 2013) and the MERRA-2 (Modern-Era Retrospective
122 Analysis for Research and Applications, version 2; Gelaro et al., 2017) fraction of AOD that is due
123 to dust (MDF). In Gkikas et al. (2021), the MDF was evaluated against the dust fraction obtained
124 from quality-assured dust and non-dust CALIOP (Cloud-Aerosol Lidar with Orthogonal Polarization;
125 Winker et al., 2009) profiles, available from the LIVAS database (Amiridis et al., 2015; Marinou et
126 al., 2017; Proestakis et al., 2018). The MDF compares well with the LIVAS dust fraction over the
127 dust-abundant areas extending across the NH dust belt, with maximum underestimations of 10 % in
128 Asian deserts. The agreement is more limited in North America and the Southern Hemisphere
129 (Figures 1 and 2 in Gkikas et al., 2021). Overall, the MIDAS DOD is well correlated with AERONET
130 dust-dominant retrievals ($R=0.89$ at global scale) and the absolute biases are mainly below 0.12 at
131 stations near sources (Figures 3 and 4 in Gkikas et al., 2021). The MIDAS DOD dataset was further
132 verified against the LIVAS DOD and compared with MERRA-2 DODs (Figure 5 in Gkikas et al.,
133 2021). Among the three datasets, there is good agreement on the monthly variability of the global and
134 hemispherical DODs as well as on their long-term averages (Figure 6 and Table 1 in Gkikas et al.,
135 2021). Moreover, the annual and seasonal DOD patterns are broadly similar in the three datasets
136 throughout the period 2007 – 2015. Nevertheless, regionally differences are found due to the different
137 techniques (passive and active remote sensing, numerical simulations) applied for the DOD
138 derivation.

139

140

141 **3. Spatiotemporal averaging and propagation of grid-cell level uncertainties**

142 In section 4.2 we provide DOD estimates that are averaged in space (regionally and globally) and
143 in time (over months, seasons and years) along with their respective uncertainties. Averaging is
144 performed according to the upper branch of Figure 5 in Levy et al. (2009), i.e. spatial averaging is
145 performed after grid cell temporal averaging for any of the timescales considered. The uncertainties
146 of the DOD averages at the different spatiotemporal scales are based on the propagation of the daily
147 grid cell uncertainties provided within the MIDAS dataset and presented in Gkikas et al. (2021). In
148 short, the daily grid cell uncertainties combine the uncertainties of the MODIS AOD and the
149 MERRA-2 MDF with respect to AERONET and LIVAS, respectively. The former is based on linear
150 equations expressing the uncertainty with respect to AERONET AOD over ocean (Levy et al., 2013)
151 and land (Levy et al., 2010; Sayer et al. 2013) with updated coefficients for C061 data depending on
152 vegetated and arid surface types (see equations 4 to 7 in Gkikas et al., 2021). The latter is based on a
153 quartic (fourth degree) polynomial equation expressing the uncertainty with respect to the LIVAS
154 dust fraction (see equation 8 in Gkikas et al., 2021).

155 In order to estimate the uncertainties of the spatiotemporal averages we first assume that each of
156 the daily grid cell uncertainties are composed of (1) a fraction that is completely random in time and
157 space, (2) a fraction that is systematic (correlated) in time and random in space and (3) a fraction that
158 is systematic (correlated) in space and random in time. Our framework also assumes that the fraction
159 of the daily grid cell uncertainty that is correlated both in space and time, for instance an instrument
160 bias, is very small and therefore neglected. Under this framework, the propagation of uncertainty
161 fraction (1) is negligible across the spatiotemporal scales considered, the propagation of uncertainty
162 fraction (2) depends upon the size of the domain considered but is negligible at global scale and across
163 most of the regional domains considered in this study, and propagation of fraction (3) accounts for
164 most of the total average uncertainty. Since we cannot know fractions (1), (2) and (3) and (1) and (2)
165 are negligible or small, we assume that (3) represents 100 % of the uncertainty, i.e the grid cell
166 uncertainty is systematic (correlated) in space and random in time, to provide an upper limit on the
167 uncertainty. In addition, we also take into account the sampling uncertainty when temporally
168 averaging over each grid cell using the standard error, i.e., we take the standard deviation divided by
169 the square root of the number of measurements.

170 In practice, when averaging the daily values for every grid cell i over months, seasons, or years,
171 the uncertainty σ'_i is obtained by adding in quadrature the daily uncertainties $\sigma_{N_i}^2$ and dividing by the
172 number of available daily measurements N_i :

$$\sigma'_i = \sqrt{\frac{\sigma_{i,1}^2 + \sigma_{i,2}^2 + \dots + \sigma_{N_i}^2}{N_i}} \quad (\text{Eq. 1})$$

175 In addition, we add in quadrature σ'_i and the standard error SE_i to obtain the total uncertainty of
176 the temporal average σ_i for every grid cell:

177

$$\sigma_i = \sqrt{\sigma'^2_i + SE_i^2} \text{ (Eq. 2)}$$

179

$$SE_i = \frac{SD_i}{\sqrt{N_i}} \text{ (Eq. 3)}$$

180
181 where SD_i is the standard deviation of the daily values in grid cell i . The standard error measures how
182 far the sample mean could be from the true population mean.

183 Finally, when spatially averaging globally or regionally, under the assumption that the errors are
184 correlated across space, the overall uncertainty is calculated by averaging σ_i across the N_j grid cells
185 in spatial domain j weighted by the grid cell area fraction with respect to the total area (i.e., grid cell
186 / total area = w_i) with available retrievals:

187

$$\sigma_j = \sum_{i=1}^{N_j} w_i * \sigma_i \text{ (Eq.4)}$$

189
190 **4. Results**

191
192 Our analysis is divided in two main parts. In the first one (Section 4.1) we assess the annual and
193 seasonal climatological DOD maps for nine distinct regions. In the second one (Section 4.2),
194 emphasis is given on the quantification of DOD averages along with their monthly and interannual
195 variability of the fractional contribution to the AOD, from a global to hemispherical level as well as
196 for specific regional domains.

197
198 *4.1 Annual and seasonal geographical distributions of DOD*

199
200 *4.1.1 North Africa, Tropical Atlantic Ocean and Mediterranean*

201
202 According to the long-term average map (Fig. 1), the maximum DODs (up to 1.2) are recorded in
203 the Bodélé depression, which is considered the most active individual dust source of the planet
204 (Washington et al., 2003; Koren et al., 2006; Ginoux et al., 2012). Over the area, the prevailing strong
205 winds are intensified further between the Tibesti mountains and the Ennedi ridge (Washington et al.,
206 2009) forming a low-level jet (Washington and Todd, 2005). This dominant wind pattern, affected
207 by the local topography (Washington et al., 2009), acts as the driving force mobilizing mineral
208 particles from arid and erodible soils of the region (Tegen et al., 2006). Under these favorable

209 conditions, dust aerosols are easily uplifted and accumulated in the atmosphere thus causing the very
210 high DODs (> 0.5) observed in the broader area (Chad, Niger). Throughout the year, the high DOD
211 levels are quite persistent exhibiting, however, a seasonal variation with more intense loads recorded
212 during DJF (Fig. S1-i) and MAM (Fig. S1-ii) following the annual cycle of source activation
213 (Washington et al., 2009). The second hotspot in N. Africa is situated between the northern parts of
214 Nigeria and the southern parts of Niger with annual DODs reaching up to 0.7 (Fig. 1) while on
215 seasonal basis vary from 0.4 (SON; Fig. S1-iv) to 0.8 (JJA; Fig. S1-iii). MIDAS DODs match well
216 with those presented by Rajot et al. (2008), who relied on ground-based sunphotometric
217 measurements of AOD obtained at the Banizoumbou AERONET site. Very high DODs are also
218 evident along the coasts of the Gulf of Guinea, which may be unrealistic considering that dust aerosols
219 are mainly transported there and are mixed with anthropogenic and biomass burning (Knippertz et
220 al., 2015). Along this area of high DODs, MERRA-2 also overestimates the dust fraction compared
221 to LIVAS (Gkikas et al., 2021) thus resulting in higher intensities according to the applied
222 methodology (Section 2). Moreover, the temporal availability of DODs in the region is very limited
223 ($<10\%$; Fig. 8-c in Gkikas et al., 2021), the DOD uncertainty is large and AOD outliers, either realistic
224 or cloud contaminated, can yield exceptional high DODs in this complex environment where aerosol
225 and clouds are spatially correlated (Andrew Sayer, personal communication). This abrupt reduction
226 of DOD levels, from inland to the nearby maritime environment, reveals an artifact of the MIDAS
227 dataset mainly introduced by the raw MODIS AOD retrievals, which are obtained by retrieval
228 algorithms built on different assumptions/considerations depending on the underlying surface type.

229 Across the Sahara Desert, there is a distinct longitudinal contrast with more intense dust loads in
230 western North Africa than in eastern North Africa (Fig. 1). In the former sector, the DODs range
231 mainly from 0.3 to 0.6 while over the eastern parts of the Sahara the corresponding limits are bounded
232 between 0.1 and 0.3 without revealing significant intra-annual variation. During MAM (Fig. S1-ii),
233 along the southern Sahel, the activation of dust sources results in DODs which locally can exceed
234 0.8, while during boreal summer (Fig. S1-iii) a vast area of the western Sahara is under the impact of
235 heavy dust loadings ($DOD > 0.5$). According to Ginoux et al. (2012), in the former region, dust is
236 mainly produced by agricultural activities (cultivation, overgrazing) disturbing soils in which alluvial
237 sediments have been accumulated. Northwards, dust has natural origin and the accumulation of
238 mineral particles is favored by the development of the Saharan Heat Low (SHL) affecting also the
239 prevailing airflow (harmattan winds) as well as the West African Monsoon (WAM) (Schepanski et
240 al., 2017). Under these meteorological conditions, several dynamic processes, from mesoscale to
241 microscale, are taking place triggering dust emission (Knippertz and Todd, 2012) from highly active
242 sources (Schepanski et al., 2007).

243 Under the impact of the trade winds, Saharan dust can travel across the tropical Atlantic Ocean
244 reaching the Caribbean Sea, the southern United States and northeastern South America (Prospero,
245 1999; Prospero et al., 2014). The signal of this long-range transport is evident on the annual
246 climatological pattern (Fig. 1) with DODs up to 0.6 (off the western Saharan coasts) fading down to
247 0.1 at the maximum distance. Within the course of the year, the Saharan dust plume varies in terms
248 of intensity, range and latitudinal position, as it is depicted in Figure S1. During boreal summer (Fig.
249 S1-iii), the corridor of the transatlantic dust transport is bounded between 10° N and 20° N latitudes
250 whereas both the intensity (DODs up to 0.6) and the range are maximized. During boreal winter (Fig.
251 S1-i), the dust zone migrates southwards (between Equator and 10° N) while maximum (up to 0.6)
252 and considerable (0.1-0.2) DODs are observed over the Gulf of Guinea and mid-Atlantic (45° W),
253 respectively. Between the transition seasons (Fig. S1-ii, S1-iv), dust loads are stronger in MAM
254 (~0.45), mainly residing within 5° N and 20° N latitudes, in contrast to SON (~0.3) when are shifted
255 northwards (10° N and 25° N). According to the existing literature, several factors modulate the
256 westwards propagation of dust plumes, originating in the western Sahara and the Bodélé Depression,
257 over the tropical Atlantic. For instance, the south-north displacement of the Saharan plumes is driven
258 by the location of the Intertropical Convergence Zone (ITCZ) and the disturbances of the African
259 easterly jet (Knippertz and Todd, 2012; Doherty et al., 2012). Teleconnection patterns, such as the El
260 Niño–Southern Oscillation (ENSO; Prospero and Lamb, 2003), the North Atlantic Oscillation (NAO;
261 Ginoux et al., 2004) and the North African Dipole Index (NAFDI; Rodríguez et al., 2015) have been
262 also studied in order to interpret the decadal variations of dust concentrations over the Atlantic.
263 Likewise, the vegetation coverage across the Sahel as well as the wind speeds, determined by the
264 prevailing atmospheric circulation, over the Sahara play a key role on the amount of the emitted dust
265 particles.

266 Due to the vicinity of the largest deserts of the planet, the Mediterranean is affected by dust
267 outbreaks throughout the year (Gkikas et al., 2013; 2016; Marinou et al., 2017). Mineral particles
268 originating primarily from north African and secondarily from Middle Eastern deserts are transported
269 towards the Mediterranean mainly under the prevalence of cyclonic systems (Gkikas et al., 2015).
270 The intensity of dust loads decreases for increasing latitudes, forming a distinct south-north gradient
271 with DODs up to 0.20 between the gulfs of Gabes (Tunisia) and Sidra (Libya), according to the annual
272 pattern (Fig. 1). Among seasons (Fig. S1), DODs vary on the locations where the maximum levels
273 are recorded as well as on their magnitude, attributed to the position of the prevailing synoptic systems
274 (Gkikas et al., 2015). The central and eastern Mediterranean sectors are affected by dust loads mainly
275 in spring (DODs up to 0.3; Fig. S1-ii) and winter (DODs up to 0.12; Fig. S1-i). In summer (Fig. S1-
276 iii), dust activity is more pronounced in the western parts with optical depths up to 0.18 (Alboran
277 Sea), while thanks to the fine resolution product, “hotspots” of similar DODs can be identified in the

278 southern parts (Andalucia) of Spain. In SON (Fig. S1-iv), dust loads are found in the central
279 Mediterranean with DODs lower than 0.12 off the Tunisian and Libyan coasts.

280

281 *4.1.2 Middle East*

282

283 In the Middle East, there is a zone of moderate-to-high DODs (locally up to 0.8) extending from
284 Mesopotamia to the southern parts of the Saudi Arabia, where one of the largest sand deserts of the
285 world (Rub' al Khali) (Hamidi et al., 2013) is situated (Fig. 2). Based on Ginoux et al. (2012), the
286 origin of mineral particles between Tigris and Euphrates as well as across the Rub' al Khali Desert is
287 mainly natural while in the intermediate part (Ad-Dahna Desert) dust accumulation is attributed to
288 the mixing of anthropogenic and hydrological sources. Slightly higher maximum DODs (up to 0.7;
289 Fig. 2) are recorded in Oman and particularly between Dhofar and Al Wusta, in contrast to previous
290 studies (Pease et al., 1998) which have identified the Wahiba Sands area as a major dust source or the
291 coastal areas of Yemen (Ginoux et al., 2012). On a seasonal basis, the intensity of mineral loads
292 exhibits a strong variability with minimum DODs (up to 0.4) during DJF (Fig. S2-i) and SON (Fig.
293 S2-iv) and maximum (up to 1) during the dry period of the year (Figs S2-ii, S2-iii), being in agreement
294 with the results presented in Yu et al. (2013). More specifically, across the Arabian Peninsula, the
295 increase in DOD levels is getting evident in boreal spring and it is further intensified during summer
296 months. Dust storms emanating in Iraq and the eastern parts of Saudi Arabia favor dust transport
297 towards the Persian Gulf (Gianakopoulou and Toumi, 2012) account for the considerable high DOD
298 levels (>0.6) found there. Due to convergence of the northern-northernwesterly Shamal winds (Yu et
299 al., 2016) and the airflow from the subtropical anticyclone, in JJA, mineral particles are travelling at
300 even longer distances towards the northern Arabian Sea (Ramaswamy et al., 2017), as indicated by
301 the intense dust loads (DODs up to 0.5; Fig. S2-iii) contributing about half of the AOD (Jin et al.,
302 2018). Likewise, during boreal summer, short-range dust transport takes place off the coasts of Oman
303 and Yemen (Gulf of Aden). Among seas in the vicinity of the Arabian Peninsula, the most intense
304 dust loads are observed in the Red Sea, forming a clear latitudinal gradient on annual (Fig. 2) and
305 summer (Fig. S2-iii) geographical DOD patterns, as it has been noted also in Brindley et al. (2015)
306 and Banks et al. (2017). Due to its location, the southern sector of the Red Sea receives dust aerosols
307 either originating from the Republic of Sudan or from the Arabian Peninsula, depending on the zonal
308 airflow (Banks et al., 2017). Dusty air masses travelling westwards are uplifted when they are
309 crossing the mountain range in the southwestern Arabian Peninsula and for this reason dust loads
310 over the southern basin are suspended above 2 km (Banks et al., 2017). On the contrary, low-elevated
311 dust layers are recorded when winds blow from west, triggering dust emission from the Tokar Gap
312 (Sudanese coasts) and subsequently dust outflows into the southern Red Sea (Banks et al., 2017).

313

314 4.1.3 *Central and southwest Asia*

315

316 Northwards and eastwards of the Caspian Sea, various deserts are situated in the central segments
317 of the Asian continent. Most part of Turkmenistan is occupied by the Karakum Desert while the
318 Kyzylkum Desert is located in Uzbekistan. Other arid regions stretch between the Caspian and Aral
319 Seas (Ustyurt plateau), in the eastern and southern flanks of the Aral Sea (Solonok Desert) and in the
320 lowlands of western Kazakhstan and southeastern Russia (Ryn Desert) (Elguindi et al., 2016). Based
321 on our seasonal spatial patterns (Fig. S3), the major dust activity is recorded in the Ustyurt Plateau
322 (Li and Sokolik, 2018) and in the large lagoon embayment of Garabogazkol (Shen et al., 2016), a gulf
323 of Turkmenistan dried into a salt-covered playa (Gills, 1996), with minimum (in DJF and SON) and
324 maximum (in MAM and JJA) DODs equal to ~0.2 and ~0.4, respectively. In the rest of areas, the
325 corresponding upper limits can reach up to 0.8-0.9, during boreal summer, in localized spots
326 (Chimboy Lake, Sarygamsh Lake) across the Karakum and Kyzylkum Deserts. In the same season,
327 moderate dust loadings (DOD up to 0.25) are encountered in the southern Caspian Sea (Elguindi et
328 al., 2016) as the result of transported mineral particles mainly coming from the sandy deserts of
329 Turkmenistan (Xi and Sokolik, 2015), under the impact of eastern/southeastern winds (Shen et al.,
330 2016). Since the 1960s, the anthropogenic intervention (agricultural activities, over-irrigation) caused
331 the retreat of the Aral Sea and the formation of the Aralkum Desert (Saiko and Zonn, 2000; Micklin,
332 2007) from which large amounts of aeolian dust are emitted and travel distances of hundreds of
333 kilometers (Indoitu et al., 2015). According to the annual climatological map (Fig. 3), extremely high
334 DODs (> 1) are found in the southeastern parts of the Aralkum Desert (Fig. 3) which are also
335 persistent among the seasons (Fig. S3). Nevertheless, these are not trustworthy as it has been
336 thoroughly discussed in Gkikas et al. (2021) (see Section 4.3.1).

337 In the Sistan basin, extending between Iran-Pakistan-Afghanistan, the long-term average JJA
338 DODs can reach up to 1.1 (Figure S3-iii) in the Margo Desert (Afghanistan), due to the frequent
339 occurrence of dust storms (Middleton, 1996), triggered by the northerly Levar winds, blowing from
340 June to September (Alizadeh Choobari et al., 2014). These maximum DOD levels are substantially
341 higher than the annual mean (0.8; Figure 3) as well as against the corresponding averages for the
342 other seasons. Thanks to the high-resolution MIDAS DOD, we identify the borders of other active
343 arid regions, surrounded by mountain ranges, such as the Rigestan (Afghanistan), the Balochistan
344 (Pakistan), the Dasht-e-Kavir (Iran), the Dasht-e-Lut (Iran) and the Jazmurian drainage basin (Iran).
345 In the aforementioned topographic lows, the magnitude of the dust loads is significantly lower than
346 those observed in the Margo Desert and can be as large as 0.6 (Balochistan) during hot-dry months
347 (Figure S3-iii). The presence of absorbing mineral particles, over the area and in the northernmost

348 part of the Arabian Sea, is also confirmed by the high AI values, especially in June-July, discussed
349 by Rashki et al. (2015), who relied on long-term records obtained by the OMI and TOMS spaceborne
350 sensors.

351

352 *4.1.4 Indian subcontinent*

353

354 In the Indian subcontinent, the maximum annual DODs (~0.5; Fig. 4) are observed along the Indus
355 river basin, in the western side of the Thar Desert whereas a branch of gradually decreasing DODs,
356 along the Indo-Gangetic plain towards eastwards directions, is also evident. Ginoux et al. (2012)
357 stated that much of dust activity in the Indus river basin is attributed to the suspension of soil particles
358 originating primarily from agricultural land use and to a lesser extent from the desiccation of
359 ephemeral water bodies. The strong presence of absorbing coarse particles over the area is further
360 supported by the coexistence of considerably high Aerosol Index (AI) values (Alam et al., 2011). As
361 indicated by the seasonal patterns (Fig. S4), the processes regulating the suspended dust loads are
362 highly variable during the year causing a remarkable temporal variability of DOD, which is low (<0.3)
363 in DJF and SON, moderate in MAM (<0.5) and maximum in JJA (<0.8). Similar seasonal variability
364 is evident in the Thar Desert, in agreement with the findings of Proestakis et al. (2018) and Dey and
365 Di Girolamo (2010), who used vertically-resolved (CALIOP) and multi-angle (MISR) satellite
366 retrievals, respectively. Nevertheless, our climatological DODs are higher with respect to the
367 CALIOP corresponding values and the MISR non-spherical AODs, particularly when dust activity
368 over the area is pronounced. During the pre-monsoon season, westerly to northwesterly winds are
369 blowing over the Thar Desert mobilizing dust particles which subsequently are advected towards the
370 Indo-Gangetic basin (Dey et al., 2004; Srivastava et al., 2011). According to our results, between the
371 Haryana state and the eastern parts of the plain, DODs fade down from ~0.6-0.7 to ~0.1-0.2, forming
372 a NW-SE gradient (Figs. S4-ii, S4-iii). Such high DODs are attributed to the eastwards propagation
373 of intense dust storms having a strong signature on the optical, microphysical and radiative properties
374 derived by AERONET stations operating in the region (Prasad et al., 2007a; Prasad et al., 2007b; Eck
375 et al., 2010).

376

377 *4.1.5 East Asia and North Pacific Ocean*

378

379 Northwards of the Tibetan Plateau is located the Tarim Basin (northwest China) in which one of
380 the largest natural dust source resides, the Taklamakan Desert. This elevated desert area (average
381 elevation 1.1 km) is surrounded by the Pamir Plateau (average elevation 5.5 km) in its west side, by
382 the Kunlun Shan range (average elevation 5.5 km) in its southern flanks and by the Tian Shan range

383 (average elevation 4.8 km) along its northern boundaries while only in its eastern margin the ground
384 elevation is low (Ge et al., 2014). DODs are maximized in spring (Fig. S5-ii) yielding values up to 1
385 along the foothills of the Tian Shan and Kunlun Shan ranges, attributed to the role of the topography
386 on winds strengthening (Ge et al., 2014). Similar values are recorded in JJA (Fig. S5-iii) but the
387 geographical distribution reveals that the highest DODs are less widespread in contrast to spring.
388 Throughout the year, the weaker dust loads are recorded during winter and autumn. Our results are
389 consistent with relevant studies that rely on active and passive satellite retrievals either of pure dust
390 load (Proestakis et al., 2018) or AOD (de Leeuw et al., 2018; Sogacheva et al., 2018).

391 A common feature in the seasonal DOD patterns is the reduction of dust loads' intensity towards
392 the interior parts of the Taklamakan Desert, as it has been also documented by Ge et al. (2014), who
393 utilized MISR retrievals. The high-resolution of the MIDAS DOD dataset provides in detail the
394 spatial information of these geographical patterns. During spring, similar high DODs to those found
395 over the Taklamakan Desert are recorded in the Qaidam Basin (northeast side of the Tibetan Plateau),
396 surrounded by the Altun, Kunlun, Qilian mountain ranges, attributed to strong downslope winds
397 causing the erosion of soil particles (Rohrmann et al., 2013) and their entrainment into the
398 atmosphere. The intensity of dust loads over the Gobi Desert (north China – south Mongolia) hardly
399 exceeds 0.3 on an annual basis (Fig. 5) while it can reach up to 0.4 during spring (Fig. S5-iii). The
400 remarkable deviations in dust abundance between Taklamakan and Gobi during springtime are
401 interpreted by variations in soil characteristics. More specifically, Taklamakan is composed mainly
402 by fine sand particles in contrast to the rocky soils of the Gobi Desert (Sun et al., 2013). Due to these
403 differences in soil textures, dust particles from the former desert region can be emitted even with low
404 wind speeds while they are uplifted at higher elevations in the troposphere, as it has been shown with
405 MISR stereo observations (Yu et al., 2019) and CALIOP lidar profiles (Proestakis et al., 2018). The
406 injection of Taklamakan dust particles at higher altitudes increase their residence time inducing also
407 their entrainment into the upper-level westerly airflow, around at 4 a.m.s.l., both contributing to the
408 higher potential for long-range transport (Yu et al., 2019), in contrast to Gobi dust, towards the
409 continental E. Asia and the northern Pacific Ocean. Under the impact of cold fronts, propagating
410 eastwards (Eguchi et al., 2009) in spring, air masses carrying mineral particles, during the first two
411 days of dust transport, affect a wide area of China (Yu et al., 2019), from near sources to its eastern
412 parts, through the Hexi Corridor and the Loess Plateau (DODs ranging from 0.2 to 0.4; Fig. S5-iii).
413 Subsequently, the Asian dust plumes are suspended over the Yellow Sea, the Korean Peninsula and
414 further eastwards, in a latitudinal band bounded between the parallels 30°N and 45°, reaching the
415 west coasts of the United States (Yu et al., 2008). Across this “belt”, where the Trans-pacific dust
416 transport is taking place, the springtime DODs decrease smoothly from 0.15 to 0.05 (Fig. S5-ii). In
417 summer (Fig. S5-iii), DODs up to 0.05 are observed between 40° N and 60° N indicating a northwards

418 displacement of the Asian dust layers (mainly originating from the Gobi Desert) due to the weakening
419 and northwards shift of the polar jet streams (Yu et al., 2019).

420

421 *4.1.6 North America*

422

423 Across N. America, the major dust activity is detected in southwest United States and in northwest
424 Mexico with annual and seasonal DODs hardly exceeding 0.15, as illustrated in Figures 6 and S6,
425 respectively. These weak dust load intensities are mainly recorded in the Sonoran and the Mojave
426 Deserts while lower values are found in the Chihuahuan Desert in which isolated spots (e.g. White
427 Sands Desert) become visible thanks to the high-resolution of the MIDAS DOD dataset. Low-to-
428 moderate DODs are evident in the Great Plains with local maxima (exceeding 0.2 in spring; Fig. S6-
429 ii) in the Great Salt Lake Desert and in the surrounding area as well as in the Baja Californian Desert
430 (Mexico; DODs up to 0.14), residing in the western side of the Gulf of California. Our annual spatial
431 distribution of DOD (Fig. 6) is highly consistent with those of frequency of observation (FoO) of
432 DOD (Ginoux et al., 2012; Baddock et al., 2016) and AI given by Prospero et al. (2002). Moreover,
433 the increase of dust loads' concentration in MAM (Fig. S6-ii), has been also documented by Hand et
434 al. (2016) and Tong et al. (2017), both relying on aerosol observations acquired at numerous stations
435 of the Interagency Monitoring of Protected Visual Environments (IMPROVE) network. During
436 springtime, dust emission over the broader area is associated with the transmit of Pacific cold fronts
437 inducing dust-entraining winds as the result of pressure gradient enhancement (Rivera Rivera et al.,
438 2009). The geomorphological soil characteristics are determinant for dust emission with the most
439 prominent natural sources being ephemeral and dry lakes (Baddock et al., 2016) while anthropogenic
440 dust aerosols are mainly emitted in the Great Plains and in the eastern side of the Gulf of California
441 (Ginoux et al., 2012).

442

443 *4.1.7 Australia*

444

445 Earlier studies based on unconstrained numerical simulations (Tanaka and Chiba, 2006; Wagener
446 et al., 2008) have shown that among the desert areas of the S. Hemisphere, the largest contribution of
447 dust particles arises from Australia. However, a more recent assessment (Kok et al., 2021b) in which
448 dust models have been constrained by observations revealed that the emitted dust amounts from S.
449 America are slightly higher than those of Australia. Due to the fairly bright landmasses and the
450 predominance of weak aerosol loadings, there is minimal contrast between surface and atmosphere
451 leading to systematic algorithm uncertainties, which can explain the slightly lower land DODs than
452 those recorded in the surrounding oceanic regions (Fig. 7 and S7). Nevertheless, in the sources as

453 well as in areas affected by dust plumes the atmospheric signal becomes evident. In particular, the
454 highest dust emissions are encountered in the Lake Eyre Basin (LEB; Prospero et al., 2002) composed
455 by ephemeral lakes, alluvial channels, gibber (stone-covered plains), aeolian sand deposits and
456 bedrocks (Bullard et al., 2008). Based on the annual climatological pattern (Fig. 7), DODs can locally
457 exceed 0.2 (in the southern parts) but in general vary between 0.06 and 0.12. From a seasonal
458 perspective (Fig. S7), the highest DODs (mainly up to 0.18 in the Warburton River estuary, few
459 exceedances above 0.4 are found in local spots) are recorded during austral summer (DJF; Fig. S7-i)
460 and spring (SON; Fig. S7-iv). Similar seasonal variation in ground-based sunphotometric
461 observations at nearby sites (Birdsville, Tinga Tingana), with slightly lower AODs, has been reported
462 by Mitchell et al. (2017). Southwards of the LEB, three spots of notable DODs (up to 0.2 in SON;
463 Fig. S7-iv) are identified in the Lakes Gairdner, Torrens and Frome while northeastwards (Lake
464 Yamma Yamma) and northwards (Simpson Desert) from the basin the suspended dust loads exhibit
465 optical depths as large as 0.12 during the driest months of the year. Similar maximum DODs are
466 recorded in the Northern Territory and in the western side of the Great Dividing Range (Queensland)
467 and in contrast to Ginoux et al. (2012) these levels appear in DJF instead of SON. In the southwestern
468 coastal parts of the Australian landmass as well as in Riverina (southeast), during austral spring (Fig.
469 S7-iv) very low DODs are evident associated with anthropogenic dust originating from agricultural
470 activities (Ginoux et al., 2012). Finally, during the same season, weak signals (DODs up to 0.05) of
471 dust transport are revealed over the Tasman and Timor Seas attributed to the eastward movement of
472 cyclonic frontal systems causing the entrainment of mineral particles in air masses that can travel at
473 long distances (Knight et al., 1995; Choobari et al., 2012).

474

475 4.1.8 *South Africa*

476

477 Dust activity in S. Africa is mainly related with short-range and short-lived plumes (Vickery et
478 al., 2013) that are suspended at low tropospheric altitudes (below 600 hPa) due to the predominance
479 of anticyclonic circulations inhibiting the vertical extension of dust layers (Piketh et al., 1999).
480 Mineral aerosol loadings are mainly originating from the ephemeral lake basins of the Etosha Pans
481 (Namibia) and Makgadikgadi Pans (Botswana) and the Namib Desert (Bryant et al., 2007; Vickery
482 et al., 2013). In the aforementioned source areas, the maximum annual (Figure 8) and seasonal (Figure
483 S8) DODs are equal to 0.1 and 0.16, respectively. Throughout the year, the increase of DODs in
484 Etosha and Makgadikgadi Pans is evident primarily in DJF (Figure S8-i) and secondarily in SON
485 (Figure S8-iv). Our results are consistent with those provided by Ginoux et al. (2012) and Bryant et
486 al. (2007) for the former region (including also the Kalahari Desert in which very weak dust loads are
487 recorded), contradictory for the latter one and opposite with the findings of Vickery et al. (2013) for

488 both sources. In these arid areas dust emission is linked with lakes' inundation, characterized by
489 strong intra-annual variability, playing an important role when different time periods are considered.
490 However, it must be also taken into account the moderate performance of the MERRA-2 dust portion
491 with respect to LIVAS in S. Africa as well as in most desert areas of the S. Hemisphere (Gkikas et
492 al., 2021). Along the Namibian coastline, the deviations of DOD between the high- and low-dust
493 seasons are small indicating that dust activity remains relatively constant within the course of the year
494 (Ginoux et al., 2012). Soil particles from salt pans and dry river beds of the Namib Desert are emitted
495 from aeolian processes related to bergwinds (katabatic winds) blowing in the escarpment, from the
496 Central Plateau down to the coasts (Eckardt and Kuring, 2005). Dust outflow towards the Southern
497 Atlantic Ocean, with a SE-NW orientation, it is shown between 18° S and 9° S during austral winter
498 (DODs up to 0.08; Fig. S8-iii), becoming more evident in SON (Fig. S8-iv), being in agreement with
499 the geographical distributions provided by Voss and Evan (2020). Such transport is favored by the
500 propagation of barotropic low-level easterly waves formed between continental high pressure systems
501 and the semi-permanent South Atlantic anticyclone (Tyson et al., 1996). Finally, weak signals of
502 DODs are recorded in the croplands north of Cape Town, with annual and DJF DODs not exceeding
503 0.1.

504

505 4.1.9 *South America*

506

507 In South America, the most intense dust loads are encountered in the Patagonia Desert where the
508 most active dust sources are situated in the river basins of the Rio Negro and Chubut provinces and
509 in its southern end. Among these areas, higher DODs (up to 0.16 in DJF; Figure S9-i) are found along
510 the Rio Negro attributed to anthropogenic dust originating from overgrazing, irrigation and oil
511 prospecting (McConnell, et al., 2007; Mazzonia and Vazquez, 2009). In southern latitudes, mineral
512 particles originate from glacier washout plains (Hernández et al., 2008). Under favorable
513 meteorological conditions, aeolian dust from Patagonia travels either towards the southern Atlantic
514 Ocean, contributing to iron concentrations and marine biological productivity in the surface waters
515 (Johnson et al., 2011), or towards the Antarctica peninsula (Gassó et al., 2010), as it has been found
516 in ice core samples (Basile et al., 1997). Both transport pathways are not visible in our climatological
517 patterns (Figures 9 and S9) since dust outbreaks are not so strong (Foth et al., 2019) while the
518 extended cloud coverage over the region results in large observational gaps of the spaceborne
519 retrievals (Gassó and Torres, 2019). Along the western side of Andes, dust emission arises from
520 natural sources located in the Sechura (Peru), Nazca (Peru) and Atacama (Chile) Deserts (Ginoux et
521 al., 2012). In the aforementioned regions, the annual DODs (Figure 9) can reach up to 0.1, 0.08 and
522 0.06, respectively, while the intra-annual variability is characterized weak (Figure S9). During MAM

523 (Figure S9-ii), DODs up to 0.16 appear in Guyana, Suriname and French Guiana as well as over their
524 offshore areas while similar intensities are evident in the northern parts of the Amazon rainforest
525 (around the Equator and bounded between 65°W and 60°W). The presence of coarse mineral particles
526 (Moran-Zuloaga, et al., 2018) over these distant areas from deserts, is attributed to the long-range
527 dust transport from North Africa across the Atlantic Ocean (Yu et al., 2015), under the impact of the
528 trade winds, taking place northwards of the convective precipitation zone formed around the ITCZ.
529 Finally, the latitudinal zone of weak DODs in the western parts of Brazil, fading down abruptly
530 eastwards of ~58° W, indicates an artifact of the MIDAS product that becomes more evident in SON
531 (Fig. S9-iv). This peculiar pattern is induced by the MERRA-2 dust fraction (results not shown here)
532 which is used for the derivation of MIDAS DOD from the MODIS AOD. An additional deficiency is
533 the relatively large DODs over an area where biomass burning particles, emitted at enormous amounts
534 by extended wildfires, clearly dominate over other aerosol species. Under these conditions, the non-
535 dust AODs are very high as well as their relevant uncertainties (Eqs. 5-7 in Gkikas et al. (2021)) while
536 the reliability of the MERRA-2 dust fraction downgrades there (see Fig. 2 in Gkikas et al. (2021)).
537

538 4.2 DOD averages and variability at global, hemispherical and regional scales

539

540 In this section, we discuss the average AOD and DOD along with their monthly and interannual
541 variability at global, hemispherical and regional scales. The left column of Figure 10 shows the
542 interannual timeseries of AOD (black curve) and DOD (red curve) averaged over the whole globe
543 (upper panel; GLB), the Northern Hemisphere (middle panel; NHE) and the Southern Hemisphere
544 (bottom panel; SHE). The right column of Figure 10 depicts the monthly seasonal cycle of AOD and
545 DOD along with the DOD-to-AOD ratio (blue curve) while the shaded areas correspond to the total
546 uncertainty (see Section 3.2 in Gkikas et al. (2021) and Section 3 in the current study).

547 The significant role of dust particles in the global aerosol budget becomes evident by visually
548 inspecting the AOD and DOD interannual timeseries (Fig. 10 i-a). The monthly contribution of
549 suspended dust to the total AOD varies from 14% to 39%, with minimum values mainly in DJF and
550 maximum values in MAM or JJA, depending on the year. Monthly DODs range from 0.016 ± 0.013
551 (Dec 2005) to 0.063 ± 0.028 (Mar 2012), whereas the long-term global annual average is equal to
552 0.032 ± 0.003 (Table 1). The global DOD mean, computed here from the fine resolution data, is
553 almost identical with those obtained by the coarse spatial resolution MERRA-2 and MIDAS DODs
554 and slightly higher than those calculated based on LIVAS-CALIOP (0.029) (see Table 1 in Gkikas et
555 al. (2021); it is noted the three datasets had been collocated based on the spatial resolution and the
556 temporal availability of the LIVAS dataset). Likewise, our global average and uncertainty computed
557 over the period 2004-2008 (0.033 ± 0.004) is close to the one obtained in Ridley et al. (2016) (0.030

558 ± 0.005), despite the different methods applied for the derivation of DOD and its uncertainty. Our
559 global DOD long-term average is very close to the CALIOP derived value (0.029) and about half of
560 the MODIS derived one (0.063) reported by Song et al. (2021).

561 Our continental (0.070 ± 0.005) and oceanic (0.019 ± 0.002) mean DODs (see Table 1) are
562 substantially lower than those obtained in Voss and Evan (2020) (land: 0.1; ocean: 0.03). This
563 difference may be attributed to the different averaging approaches, which can have an important
564 impact on the calculations as it has been shown in Levy et al. (2009) (see their Figure 5). Based on
565 our method, we are giving the same “weight” at each grid cell (regardless of the amount of available
566 data in that grid cell throughout the study period) when we are calculating the domain (from regional
567 to global) average. Therefore, we are avoiding an overestimation of the spatial average since MIDAS
568 data availability is larger over/nearby deserts (see Figure 8-c in Gkikas et al. (2021)) where the higher
569 DODs are observed. To be more specific, when we are calculating the global long-term DOD average
570 based on the second branch (i.e., “Straight”, the standard approach for the calculation of the average
571 value by considering all the available values in space and time) in Levy et al. (2009), we obtain a
572 climatological value equal to 0.047. Such different approaches for the calculation of the long-term
573 DOD averages might interpret and the deviations found between this study and Song et al. (2021).
574 Finally, the computed global mean MIDAS DOD is somewhat higher than those simulated by most
575 AeroCom Phase I models (Huneeus et al., 2011), being about 40% higher than the median (0.023);
576 nevertheless, it must be taken into account that most models account for the diurnal variation of DOD
577 in contrast to the single-measurements taken during MODIS overpass.

578 As expected, the interannual GLB DOD timeseries is driven by the variability in the NHE DOD
579 (Figure 10 ii-a) since the most widespread and intense dust sources are located in the Northern
580 Hemisphere. This is justified by their high temporal co-variation while a positive NHE-GLB offset is
581 constantly observed, being lower during boreal winter and autumn (up to 0.035) and maximum during
582 the high dust seasons (0.058). The fraction of monthly NHE AOD attributed to dust particles ranges
583 from 20% to 48% and the R^2 value between monthly AOD and DOD is equal to 0.94, both indicating
584 a dominant dust contribution. Over the study period (2003-2017), the NHE DOD yields a
585 climatological mean equal to 0.056 ± 0.004 (Table 1) ranging from 0.024 ± 0.015 (Dec 2005) to 0.121
586 ± 0.050 (Mar 2012). In contrast, marine and biomass burning aerosols, rather than dust, regulate AOD
587 in the Southern Hemisphere (Figure 10 iii-a). SHE DODs are estimated to be low (0.008 ± 0.001),
588 with the maximum value (0.016 ± 0.016) recorded in February 2016. The contribution of dust aerosols
589 to the total aerosol load does not exceed 17% throughout the study period (Fig. 10 iii-a) and on
590 average it is equal to $8.2\% \pm 1.1\%$, which is in very good agreement with the findings by Kok et al.
591 (2021b).

592 A better view of the seasonal cycles of AOD, DOD and the DOD-to-AOD ratio can be obtained
593 by investigating their climatological patterns, representative for the period of interest (2003-2017).
594 On a global scale (Fig. 10 i-b), DODs peak between March and June (~0.045), and then decline until
595 November (0.018) before rising during boreal winter. Despite the monthly shifts between maximum
596 AOD and DOD averages, the seasonal cycles of the total aerosol and dust burdens are similar to a
597 large extent, whereas the contribution of mineral particles to the total extinction ranges from 16%
598 (November) to 33% (March-June). The MIDAS global DOD-to-AOD ratio (~23%) is close to the
599 values reported by Gelaro et al. (2017) and Kinne et al. (2006), ~22% and ~26%, respectively, but
600 higher than most of the model-derived estimations (12% - 28%) from the AeroCom Phase III (Gliss
601 et al., 2021). These discrepancies, excluding the aerosol parametrizations, may be partly due to the
602 different sampling between single-overpass satellite observations and reanalyses (Gelaro et al., 2017)
603 or models (Kinne et al., 2006) where the diurnal aerosol variability (Schepanski et al., 2009; Yu et
604 al., 2021) is included. In the NHE (Fig. 10 ii-b), the mean seasonal trend of DODs remains relatively
605 unchanged when compared with GLB; however, the hemispheric means (0.030-0.088) and the dust
606 fraction (24-41%) are higher. On the contrary, the weak signal of aeolian dust in SHE (Fig. 10 iii-b)
607 interprets the very low DODs (0.005 – 0.011) and their minor impact (6-12%) upon AOD magnitude.

608 The analysis presented above has also been conducted for each one of the 17 sub-regions
609 illustrated in Figure 7 in Gkikas et al. (2021), and the main findings are summarized in this paragraph.
610 Among the regional domains, a persistency of high DODs (>0.3), both at interannual and seasonal
611 scales, it is found only in BOD, which yields a long-term average value equal to 0.533 ± 0.009 , being
612 almost double than WSA (0.302 ± 0.006) and TAK (0.246 ± 0.020) as illustrated in Table 1. However,
613 when focus is given to individual months, the maximum DODs over the study period (Fig. 11 vi-a)
614 and on their climatological levels are recorded in the Taklamakan Desert and can be as high as 0.868
615 (April 2007) and 0.600 (April), respectively. Comparable or even higher DODs than those computed
616 in BOD, are also evident for specific months in THA (Fig. 11 vii-a), GOG (Fig. 11 xii-a) and SSA
617 (Fig. 11 xv-a) as well as on the monthly timeseries (THA; Fig. 11 vii-b). Mineral particles'
618 contribution to the total AOD (i.e., blue curves in the seasonal cycle plots) is at least 50% over dust
619 sources or dust-abundant areas in N. Africa, Middle East and Asia and it is constantly higher than
620 70%, reaching up to 95%, in BOD (Fig. 11 i-b), WSA (Fig. 11 viii-b) and TAK (Fig. 11 vi-b). Over
621 downwind regions, such as EAS (Fig. 11 ix-b), GOG (Fig. 11 xii-b), MED (Fig. 11 xiii-b) and SSA
622 (Fig. 11 xv-b), the dust contribution can prevail over the non-dust portion (GOG, MED, SSA) while
623 in EAS does not exceed 30%, due to the predominance of anthropogenic aerosols. In the oceanic
624 areas of Tropical Atlantic and North Pacific, where large-scale dust transport is taking place, AOD
625 and DOD co-vary, indicating that the dust activity regulates the temporal variations of aerosols' load,
626 except during summer months in WNP (Fig. 11 xvi-a, xvi-b). Regarding the seasonal cycle of DOD,

627 the maximum values are recorded either during boreal spring (GOB, CAS, NME, SUS, TAK, EAS,
628 ENP, GOG, MED, WNP and SSA) or during boreal summer (THA, WSA, ETA, SME and WTA) or
629 are similar between the two high-dust seasons (BOD).

630 A final intercomparison of the MIDAS DODs against those derived by Ridley et al. (2016) and
631 Adebiyi et al. (2020), on a seasonal basis over the period 2004 - 2008, has been performed for 15
632 regions defined in Kok et al. (2021a) (see their Figure 2-b and Table 2). The obtained results are
633 illustrated in Figure 12. For the southern hemisphere regions (Figs. 12 –xiii, xiv, xv) as well as for
634 North America (Fig. 12-xii), MIDAS DODs are compared versus those from Adebiyi et al. (2020)
635 while for the remaining 11 domains (Figs. 12-i – xi) the results from Ridley et al. (2016) have been
636 utilized. As an overview, it is noted that the seasonal cycle among the three databases is commonly
637 reproduced, with a few exceptions (Mali-Niger, Kyzyl Kum, Southern Africa), whereas the DOD
638 uncertainties (represented by the error bars) are comparable. Regarding the magnitudes, MIDAS
639 DODs are mainly somewhat lower than those of Ridley et al. (2016) across the dust belt in contrast
640 to the outflow region of the Mid-Atlantic (Fig. 12-i). The obtained differences are mainly attributed
641 to the consideration of different models for accounting for the non-dust portion, the different
642 treatment of AODs (bias correction vs. quality filtering), the different versions of MODIS retrievals
643 (C006 vs C061), the consideration of multi-satellite observations instead of relying only on MODIS-
644 Aqua retrievals as well as to the different spatial scales (coarse vs. fine). In relative terms, the largest
645 deviations are found in the desert areas of the southern hemisphere where models struggle to represent
646 adequately the dust sources and the emitted amounts of mineral particles, thus affecting the dust
647 fraction ratio provided by MERRA-2.

648

649 **5. Summary and conclusions**

650

651 The current study presents a scientific exploitation of the MIDAS dataset (Gkikas et al., 2021),
652 which provides columnar mid-visible (550 nm) dust optical depth (DOD) at fine spatial resolution
653 ($0.1^\circ \times 0.1^\circ$) and over a 15-year period (2003 – 2017). Taking advantage of the global coverage of
654 the MIDAS DOD product, we analyzed the contribution of dust aerosols to AOD at various spatial
655 and temporal scales. More specifically, we focused on 9 regions that account for the majority of the
656 global dust budget, encompassing sources and downwind areas with the main dust transport
657 pathways. Such regions comprise the deserts extending across the “dust belt”, North America,
658 Australia, South Africa and South America as well as maritime areas (Tropical Atlantic Ocean,
659 Mediterranean, North Pacific Ocean) receiving constantly large amounts of mineral particles from
660 the nearby deserts. At a further step, the interannual and intra-annual timeseries of DODs along with

661 their contribution to the total aerosol load (AOD), were investigated at global, hemispherical and
662 regional level.

663 According to our findings, the global long-term DOD average over the study period (2003-2017)
664 is equal to 0.032 ± 0.003 , yielding a strong contrast between the contributions from the northern
665 (0.056 ± 0.004) and southern (0.008 ± 0.001) hemispheres. Our global estimations are almost identical
666 with those given by Ridley et al. (2016) and the CALIOP-derived estimate of Song et al. (2021), in
667 contrast to the MODIS-based average given from the latter study. Nevertheless, when the global
668 averages are calculated separately over land (0.070 ± 0.005) and ocean (0.019 ± 0.002), our results
669 differ substantially than those found in Voss and Evan (2020), who reported continental and maritime
670 DODs equal to 0.100 and 0.030, respectively. Such large deviations are attributed to the different
671 applied methodologies and averaging procedures followed. Moreover, we find very good agreement,
672 in terms of DOD magnitude and uncertainty, of the MIDAS seasonal DODs versus those of Ridley
673 et al. (2016) and Adebiyi et al. (2020) for 15 regions defined in Kok et al. (2021a). Considering that
674 the long-term DOD averages can be utilized for constraining global dust in climate models, or can be
675 used in several other applications, a detailed analysis is required for enlightening the factors resulting
676 in disagreements among studies. Likewise, our computed global DOD average resides around the
677 middle of the AeroCom (Huneeus et al., 2011) limits, being higher than the median (0.023) and mean
678 (0.028). However, in the model-based calculations the diurnal variability is taken into account in
679 contrast to the satellite-based estimations relying on single overpass measurements per day.

680 Regarding the dust contribution to the total aerosol optical depth, the DOD-to-AOD ratio from
681 32% at N. Hemisphere drops down to 8% in S. Hemisphere while at global scale is about one quarter
682 (23%). The contradiction found between the two hemispheres, both for DOD and dust fraction, is
683 interpreted by the most pronounced dust activity recorded in the Bodélé Depression of the northern
684 Lake Chad Basin (DODs up to ~1.2), across the Sahel (DODs up to 0.8), in western parts of the
685 Sahara Desert (DODs up to 0.6), in the eastern parts of the Arabian Peninsula (DODs up to ~1), along
686 the Indus river basin (DODs up to 0.8) and in the Taklamakan Desert (DODs up to ~1). On the
687 contrary, the weaker emission mechanisms triggering dust mobilization over the spatially limited
688 sources of Patagonia, South Africa and interior arid areas of Australia do not favor the accumulation
689 of mineral particles at large amounts (DODs up to 0.4 at local hotspots), even during high-dust
690 seasons. Except for the Bodélé Depression, where the seasonal variability of the intense dust loads is
691 relatively weak, in the other dust sources of the N. Hemisphere, DODs exhibit a strong seasonal cycle
692 with maximum levels either during boreal spring or summer and minimum in boreal winter.

693 Over oceans, the main pathways of long-range dust transport are observed along the tropical
694 Atlantic and the northern Pacific, revealing a remarkable variation, within the course of the year, in
695 terms of intensity, latitudinal position and range. Saharan dust plumes, reaching the Caribbean Sea in

696 summer under the impact of the trade winds, are more abundant with respect to Asian dust, arriving
697 at the western coasts of the United States in spring under the impact of midlatitude cyclones. Due to
698 the convergence of the Shamal winds, blowing over the Arabian Peninsula, and the wind flow from
699 the subtropical anticyclone, dust aerosols originating in the Middle East can reach the western Indian
700 coasts in summer, crossing the Arabian Sea. Dust loads in the southern parts of the Red Sea are
701 maximized during boreal summer when Saharan or Middle East dust is transported, depending on the
702 zonal airflow. The intensity of dust burden in the Mediterranean forms a south-north gradient,
703 whereas a seasonal longitudinal shift of the maximum DODs, off the northern African coasts, is
704 evident attributed to the prevailing synoptic circulation.

705 Despite the strong capabilities of the MIDAS dataset, we have also identified some
706 limitations, thoroughly discussed here and in Gkikas et al. (2021), attributed either to inherent
707 weaknesses of the raw MODIS AOD retrievals or to deficiencies of MDF, resulting in not too realistic
708 patterns in specific regions of the planet. Thanks to this detailed analysis, potential users are aware
709 of any issue that may rise when utilizing the MIDAS DOD product. Moreover, it is among our
710 priorities to minimize the impacts of these drawbacks in future versions of the MIDAS dataset.

711 As already mentioned, a variety of research studies can rely on the MIDAS dataset. MIDAS has
712 been already used for the investigation of DOD trends (Logothetis et al., 2021) whereas in a follow-
713 up study the mechanisms contributing to the temporal variations of dust burden will be investigated.
714 Likewise, the MIDAS DOD product has been utilized in radiative transfer studies (Fountoulakis et
715 al, 2021; Masoom et al., 2021) focusing on the impacts on solar energy production. Moreover, taking
716 advantage of the fine spatial resolution of the MIDAS dataset and of its extended temporal
717 availability, the dataset can be used for the identification of dust sources worldwide, similarly to the
718 analysis done in Ginoux et al. (2012). Finally, we have provided a simple, yet flexible method
719 (independent from other datasets) to calculate consistent uncertainties across spatiotemporal scales,
720 which will ease the use of the MIDAS dataset in data assimilation applications.

721

722 **Acknowledgments**

723 Antonis Gkikas acknowledges support by the Hellenic Foundation for Research and Innovation
724 (H.F.R.I.) under the “2nd Call for H.F.R.I. Research Projects to support Post-Doctoral Researchers”
725 (Project Acronym: ATLANTAS, Project Number: 544). Vassilis Amiridis acknowledges support
726 from the European Research Council (grant no. 725698; D-TECT). Eleni Marinou was funded by a
727 DLR VO-Ryoung investigator group and the Deutscher Akademischer Austauschdienst (grant no.
728 57370121). Jasper F. Kok acknowledges support from National Science Foundation (NSF) grant
729 1552519. Carlos Pérez García-Pando acknowledges support from the European Research Council
730 (grant no. 773051; FRAGMENT), the AXA Research Fund, and the Spanish Ministry of Science,

731 Innovation and Universities (grant nos. RYC-2015-18690 and CGL2017- 88911-R). The authors
732 acknowledge support from the DustClim project as part of ERA4CS, an ERA-NET project initiated
733 by JPI Climate and funded by FORMAS (SE), DLR (DE), BMWFW (AT), IFD (DK), MINECO
734 (ES), and ANR (FR), with cofunding by the European Union (grant no. 690462). PRACE (Partnership
735 for Advanced Computing in Europe) and RES (Red Española de Supercomputación) are
736 acknowledged for awarding access to the MareNostrum Supercomputer in the Barcelona
737 Supercomputing Center. We acknowledge support of this work by the PANhellenic infrastructure for
738 Atmospheric Composition and climatE chAnGe (PANACEA) project (grant no. MIS 5021516),
739 which is implemented under the Horizon 2020 Action of “Reinforcement of the Research and
740 Innovation Infrastructure”, funded by the Operational Programme Competitiveness,
741 Entrepreneurship, and Innovation (NSRF 2014–2020) and cofinanced by Greece and the European
742 Union (under the European Regional Development Fund). NOA members acknowledge support from
743 the Stavros Niarchos Foundation (SNF). The authors acknowledge support by the COST Action
744 “InDust” (grant no. CA16202), supported by COST (European Cooperation in Science and
745 Technology). The authors would like to thank Andrew Mark Sayer for his valuable and constructive
746 comments. The authors would like also to thank Thanasis Georgiou for developing the ftp server on
747 which the MIDAS data set is stored.

748

749 **Data availability**

750

751 The MIDAS dataset has been developed in the framework of the DUST-GLASS project (grant no.
752 749461; European Union’s Horizon 2020 Research and Innovation programme under the Marie
753 Skłodowska-Curie Actions) and it is available at: <https://doi.org/10.5281/zenodo.4244106>.

754

755 **References**

756 Adebiyi, A. A., Kok, J. F., Wang, Y., Ito, A., Ridley, D. A., Nabat, P., and Zhao, C.: Dust Constraints
757 from joint Observational-Modelling-experiMental analysis (DustCOMM): comparison with
758 measurements and model simulations, *Atmos. Chem. Phys.*, 20, 829–863,
759 <https://doi.org/10.5194/acp-20-829-2020>, 2020.

760 Alam, K., Qureshi, S., & Blaschke, T.: Monitoring spatio-temporal aerosol patterns over Pakistan
761 based on MODIS, TOMS and MISR satellite data and a HYSPLIT model. *Atmospheric Environment*,
762 45, 4641–4651, 2011.

763 Alizadeh-Choobari, O., Zawar-Reza, P., Sturman, A.: The “wind of 120 days” and dust storm activity
764 over the Sistan Basin, *Atmos. Res.*, 143, 328–341, 2014.

765

766 Amiridis, V., Wandinger, U., Marinou, E., Giannakaki, E., Tsekeri, A., Basart, S., Kazadzis, S.,
767 Gkikas, A., Taylor, M., Baldasano, J., and Ansmann, A.: Optimizing CALIPSO Saharan dust
768 retrievals, *Atmos. Chem. Phys.*, 13, 12089–12106, <https://doi.org/10.5194/acp-13-12089-2013>, 2013.

769

770 Amiridis, V., Marinou, E., Tsekeri, A., Wandinger, U., Schwarz, A., Giannakaki, E., Mamouri, R.,
771 Kokkalis, P., Binietoglou, I., Solomos, S., Herekakis, T., Kazadzis, S., Gerasopoulos, E., Proestakis,
772 E., Kottas, M., Balis, D., Papayannis, A., Kontoes, C., Kourtidis, K., Papagiannopoulos, N., Mona,
773 L., Pappalardo, G., Le Rille, O., and Ansmann, A.: LIVAS: a 3-D multi-wavelength aerosol/cloud
774 database based on CALIPSO and EARLINET, *Atmos. Chem. Phys.*, 15, 7127-7153,
775 <https://doi.org/10.5194/acp-15-7127-2015>, 2015.

776

777 Baddock, M. C., Ginoux, P., Bullard, J. E., and Gill, T. E.: Do MODIS-defined dust sources have a
778 geomorphological signature?, *Geophys. Res. Lett.*, 43, GL067327, doi:10.1002/2015GL067327,
779 2016.

780

781 Banks, J. R., Brindley, H. E., Stenchikov, G., and Schepanski, K.: Satellite retrievals of dust aerosol
782 over the Red Sea and the Persian Gulf (2005–2015), *Atmos. Chem. Phys.*, 17, 3987-4003,
783 <https://doi.org/10.5194/acp-17-3987-2017>, 2017.

784

785 Basile, I., Grousset, F. E., Revel, M., Petit, J.-R., Biscaye, P. E., and Barkov, N. I.: Patagonian origin
786 of glacial dust deposited in East Antarctica (Vostok and Dome C) during glacial stages 2, 4 and 6,
787 *Earth Planet. Sc. Lett.*, 146, 573–589, 1997.

788

789 Brindley, H., Osipov, S., Bantges, R., Smirnov, A., Banks, J., Levy, R., Jish Prakash, P., and
790 Stenchikov, G.: An assessment of the quality of aerosol retrievals over the Red Sea and evaluation of
791 the climatological cloud-free dust direct radiative effect in the region, *J. Geophys. Res.-Atmos.*, 120,
792 10862–10878, doi:10.1002/2015JD023282, 2015.

793

794 Bryant, R. G., Bigg, G. R., Mahowald, N. M., Eckardt, F. D., and Ross S. G.: Dust emission response
795 to climate in southern Africa, *J. Geophys. Res.*, 112, D09207, doi:10.1029/2005JD007025, 2007.

796

797 Bullard, J. E., and Austin, M. J.: Dust generation on a proglacial floodplain, West Greenland. *Aeolian*
798 Res. 3, 43–54. doi: 10.1016/j.aeolia.2011.01.002, 2011, 2017.

799

800 Bullard, J. E., Baddock, M., Bradwell, T., Crusius, J., Darlington, E., Gaiero, D., Gassó, S.,
801 Gisladottir, G., Hodgkins, R., McCulloch, R., McKenna-Neuman, C., Mockford, T., Stewart, H., and,
802 Thorsteinsson, T.: High-latitude dust in the Earth system, *Rev. Geophys.*, 54, 447–485,
803 <https://doi.org/10.1002/2016RG000518>, 2016.

804

805 Bullard, J., Baddock, M., McTainsh, G. H., and Leys, J. F.: Subbasin scale dust source
806 geomorphology detected using MODIS, *Geophys. Res. Lett.*, 35, L15404,
807 doi:10.1029/2008GL033928, 2008.

808 Chin, M., Ginoux, P., Kinne, S., Torres, O., Holben, B. N., Duncan, D. N., Martin, R. V., Logan, J.
809 A., Higurashi, H., and Nakajima, T.: Tropospheric aerosol optical thickness from the GOCART
810 model and comparisons with satellite and Sun photometer measurements, *J. Atmos. Sci.*, 59, 451–
811 483, [https://doi.org/10.1175/1520-0469\(2002\)059<0461:TAOTFT>2.0.CO;2](https://doi.org/10.1175/1520-0469(2002)059<0461:TAOTFT>2.0.CO;2), 2002.

812

813 de Leeuw, G., Sogacheva, L., Rodriguez, E., Kourtidis, K., Georgoulias, A. K., Alexandri, G.,
814 Amiridis, V., Proestakis, E., Marinou, E., Xue, Y., and van der A, R.: Two decades of satellite
815 observations of AOD over mainland China using ATSR-2, AATSR and MODIS/Terra: data set
816 evaluation and large-scale patterns, *Atmos. Chem. Phys.*, 18, 1573–1592, <https://doi.org/10.5194/acp-18-1573-2018>, 2018.

818

819 Dey, S. and Di Girolamo, L.: A climatology of aerosol optical and microphysical properties over the
820 Indian subcontinent from 9 years (2000–2008) of Multiangle Imaging Spectroradiometer (MISR)
821 data, *J. Geophys. Res.-Atmos.*, 115, D15204, <https://doi.org/10.1029/2009JD013395>, 2010.

822

823 Dey, S., Tripathi, S. N., Singh, R. P., and Holben, B. N.: Influence of dust storms on the aerosol
824 optical properties over the Indo-Gangetic basin, *J. Geophys. Res.-Atmos.*, 109, 1–10,
825 doi:10.1029/2004jd004924, 2004.

826

827 Di Tomaso, E., Schutgens, N. A. J., Jorba, O., and Pérez García-Pando, C.: Assimilation of MODIS
828 Dark Target and Deep Blue observations in the dust aerosol component of NMMB-MONARCH
829 version 1.0, *Geosci. Model Dev.*, 10, 1107–1129, <https://doi.org/10.5194/gmd-10-1107-2017>, 2017.

830

831 Doherty, O. M., Riemer, N., and Hameed, S.: Control of Saharan mineral dust transport to Barbados
832 in winter by the Intertropical Convergence Zone over West Africa: Winter dust in Barbados and the
833 ITCZ, *J. Geophys. Res.-Atmos.*, 117, D19117, doi:10.1029/2012JD017767, 2012.

834

835 Du, Y., Xu, X., Chu, M., Guo, Y., and Wang, J.: Air particulate matter and cardiovascular disease:
836 the epidemiological, biomedical and clinical evidence, *J. Thorac. Dis.*, 8, E8,
837 <https://doi.org/10.3978/j.issn.2072-1439.2015.11.37>, 2016.

838

839 Eck, T. F., Holben, B. N., Sinyuk, A., Pinker, R. T., Goloub, P., Chen, H., Chatenet, B., Li, Z., Singh,
840 R. P., and Tripathi, S. N.: Climatological aspects of the optical properties of fine/coarse mode aerosol
841 mixtures, *J. Geophys. Res.-Atmos.*, 115, 19205, <https://doi.org/10.1029/2010JD014002>, 2010.

842

843 Eckardt, F.D. Kuring, N.: SeaWiFS identifies dust sources in the Namib Desert. *International Journal*
844 of *Remote Sensing*, 26:4159–4167, 2005.

845

846 Eguchi, K., Uno, I., Yumimoto, K., Takemura, T., Shimizu, A., Sugimoto, N., and Liu, Z.: Trans-
847 pacific dust transport: integrated analysis of NASA/CALIPSO and a global aerosol transport model,
848 *Atmos. Chem. Phys.*, 9, 3137-3145, <https://doi.org/10.5194/acp-9-3137-2009>, 2009.

849

850 Elguindi, N., Solmon, F., Turuncoglu, U.: Quantifying some of the impacts of dust and other aerosol
851 on the Caspian Sea region using a regional climate model. *Clim. Dyn.*, 46, 41–55, 2016.

852

853 Fiedler, S., Schepanski, K., Heinold, B., Knippertz, P., and Tegen, I.: Climatology of nocturnal low-
854 level jets over North Africa and implications for modeling mineral dust emission, *J. Geophys. Res.-*
855 *Atmos.*, 118, 6100–6121, 2013.

856

857 Flaounas, E., Kotroni, V., Lagouvardos, K., Kazadzis, S., Gkikas, A., and Hatzianastassiou, N.:
858 Cyclone contribution to dust transport over the Mediterranean region, *Atmos. Sci. Lett.*, 16, 473–478,
859 doi:10.1002/asl.584, 2015.

860

861 Foth, A., Kanitz, T., Engelmann, R., Baars, H., Radenz, M., Seifert, P., Barja, B., Fromm, M.,
862 Kalesse, H., and Ansmann, A.: Vertical aerosol distribution in the southern hemispheric midlatitudes
863 as observed with lidar in Punta Arenas, Chile (53.2° S and 70.9° W), during ALPACA, *Atmos. Chem.*
864 *Phys.*, 19, 6217–6233, <https://doi.org/10.5194/acp-19-6217-2019>, 2019.

865

866 Fountoulakis, Ilias, Panagiotis Kosmopoulos, Kyriakoula Papachristopoulou, Ioannis-Panagiotis
867 Raptis, Rodanthi-Elisavet Mamouri, Argyro Nisantzi, Antonis Gkikas, Jonas Withuhn, Sebastian
868 Bley, Anna Moustaka, Johannes Buehl, Patric Seifert, Diofantos G. Hadjimitsis, Charalampos
869 Kontoes, and Stelios Kazadzis. 2021. "Effects of Aerosols and Clouds on the Levels of Surface Solar

870 Radiation and Solar Energy in Cyprus" Remote Sensing 13, no. 12: 2319.
871 <https://doi.org/10.3390/rs13122319>

872
873 Gassó, S., Stein, A., Marino, F., Castellano, E., Udisti, R., and Ceratto, J.: A combined observational
874 and modeling approach to study modern dust transport from the Patagonia desert to East Antarctica,
875 *Atmos. Chem. Phys.*, 10, 8287-8303, <https://doi.org/10.5194/acp-10-8287-2010>, 2010.

876
877 Gassó, S., & Torres, O.: Temporal characterization of dust activity in the Central Patagonia desert
878 (years 1964–2017), *Journal of Geophysical Research: Atmospheres*, 124, 3417– 3434.
879 <https://doi.org/10.1029/2018JD030209>, 2019.

880
881 Ge, J. M., Huang, J. P., Xu, C. P., Qi, Y. L., and Liu, H. Y.: Characteristics of Taklimakan dust
882 emission and distribution: a satellite and reanalysis field perspective, *J. Geophys. Res.-Atmos.*, 119,
883 11772–11783, <https://doi.org/10.1002/2014JD022280>, 2014.

884
885 Gelaro, R, McCarty, W., Suárez, M. J., Todling, R., Molod, A., Takacs, L., Randles, C. A., Darmenov,
886 A., Bosilovich, M. G., Reichle, R., Wargan, K., Coy, L., Cullather, R., Draper, C., Akella, S.,
887 Buchard, V., Conaty, A., da Silva, A. M., Gu, W., Kim, G., Koster, R., Lucchesi, R., Merkova, D.,
888 Nielsen, J. E., Partyka, G., Pawson, S., Putman, W., Riener, M., Schubert, S. D., Sienkiewicz, M.,
889 and Zhao, B.: The Modern-Era Retrospective Analysis for Research and Applications, Version 2
890 (MERRA-2), *J. Climate*, 30, 5419–5454, <https://doi.org/10.1175/JCLI-D-16-0758.1>, 2017.

891
892 Gill, T. E.: Eolian sediments generated by anthropogenic disturbance of playas: human impacts on
893 the geomorphic system and geomorphic impacts on the human system, *Geomorphology*, 17, 207–
894 228, 1996.

895
896 Ginoux, P., Prospero, J. M., Torres, O., and Chin, M.: Longterm simulation of global dust distribution
897 with the GOCART model: correlation with North Atlantic Oscillation, *Environ. Modell. Softw.*, 19,
898 113–128, [https://doi.org/10.1016/S1364-8152\(03\)00114-2](https://doi.org/10.1016/S1364-8152(03)00114-2), 2004.

899
900 Ginoux, P., Prospero, J. M., Gill, T. E., Hsu, N. C., and Zhao, M.: Global-scale attribution of
901 anthropogenic and natural dust sources and their emission rates based on MODIS Deep Blue aerosol
902 products, *Rev. Geophys.*, 50, RG3005, <https://doi.org/10.1029/2012RG000388>, 2012.

903

904 Gkikas, A., Hatzianastassiou, N., Mihalopoulos, N., Katsoulis, V., Kazadzis, S., Pey, J., Querol, X.,
905 and Torres, O.: The regime of intense desert dust episodes in the Mediterranean based on
906 contemporary satellite observations and ground measurements, *Atmos. Chem. Phys.*, 13, 12135-
907 12154, <https://doi.org/10.5194/acp-13-12135-2013>, 2013.

908

909 Gkikas, A., Houssos, E. E., Lolis, C. J., Bartzokas, A., Mihalopoulos, N., and Hatzianastassiou, N.:
910 Atmospheric circulation evolution related to desert-dust episodes over the Mediterranean, *Q. J. Roy.
911 Meteor. Soc.*, 141, 1634–1645, doi:10.1002/qj.2466, 2015.

912

913 Gkikas, A., Basart, S., Hatzianastassiou, N., Marinou, E., Amiridis, V., Kazadzis, S., Pey, J., Querol,
914 X., Jorba, O., Gassó, S., and Baldasano, J. M.: Mediterranean intense desert dust outbreaks and their
915 vertical structure based on remote sensing data, *Atmos. Chem. Phys.*, 16, 8609-8642,
916 <https://doi.org/10.5194/acp-16-8609-2016>, 2016.

917

918 Gkikas, A., Obiso, V., Pérez García-Pando, C., Jorba, O., Hatzianastassiou, N., Vendrell, L., Basart,
919 S., Solomos, S., Gassó, S., and Baldasano, J. M.: Direct radiative effects during intense Mediterranean
920 desert dust outbreaks, *Atmos. Chem. Phys.*, 18, 8757-8787, <https://doi.org/10.5194/acp-18-8757-2018>, 2018.

922

923 Gkikas, A., Giannaros, T.M., Kotroni, V., Lagouvardos, K.: Assessing the radiative impacts of an
924 extreme desert dust outbreak and the potential improvements on short-term weather forecasts: The
925 case of February 2015, *Atmos. Res.*, 226, 152-170, <https://doi.org/10.1016/j.atmosres.2019.04.020>,
926 2019.

927

928 Gkikas, A., Proestakis, E., Amiridis, V., Kazadzis, S., Di Tomaso, E., Tsekeri, A., Marinou, E.,
929 Hatzianastassiou, N., and Pérez García-Pando, C.: ModIs Dust AeroSol (MIDAS): a global fine-
930 resolution dust optical depth data set, *Atmos. Meas. Tech.*, 14, 309–334, <https://doi.org/10.5194/amt-14-309-2021>, 2021.

932

933 Gliß, J., Mortier, A., Schulz, M., Andrews, E., Balkanski, Y., Bauer, S. E., Benedictow, A. M. K.,
934 Bian, H., Checa-Garcia, R., Chin, M., Ginoux, P., Griesfeller, J. J., Heckel, A., Kipling, Z., Kirkevåg,
935 A., Kokkola, H., Laj, P., Le Sager, P., Lund, M. T., Lund Myhre, C., Matsui, H., Myhre, G., Neubauer,
936 D., van Noije, T., North, P., Olivié, D. J. L., Rémy, S., Sogacheva, L., Takemura, T., Tsigaridis, K.,
937 and Tsyro, S. G.: AeroCom phase III multi-model evaluation of the aerosol life cycle and optical

938 properties using ground- and space-based remote sensing as well as surface in situ observations,
939 *Atmos. Chem. Phys.*, 21, 87–128, <https://doi.org/10.5194/acp-21-87-2021>, 2021.

940

941 Hamidi, M., Kavianpour, M. R., and Shao, Y.: Synoptic analysis of dust storms in the Middle East,
942 *Asia-Pac. J. Atmos. Sci.*, 49, 279–286, 2013.

943

944 Hand, J. L., Gill, T. E., and Schichtel, B. A.: Spatial and seasonal variability in fine mineral dust and
945 coarse aerosol mass at re-mote sites across the United States, *J. Geophys. Res.-Atmos.*, 122, 3080–
946 3097, <https://doi.org/10.1002/2016jd026290>, 2017.

947

948 Haywood, J. and Boucher, O.: Estimates of the direct and indirect radiative forcing due to
949 tropospheric aerosols: A review, *Rev. Geophys.*, 38, 513–543,
950 <https://doi.org/10.1029/1999RG000078>, 2000.

951

952 Huang, J., Lin, B., Minnis, P., Wang, T., Wang, X., Hu, Y., Yi, Y., and Ayers, J. K.: Satellite-based
953 assessment of possible dust aerosols semi-direct effect on cloud water path over East Asia, *Geophys.*
954 *Res. Lett.*, 33, L19802, <https://doi.org/10.1029/2006GL026561>, 2006.

955

956 Huneeus, N., Schulz, M., Balkanski, Y., Griesfeller, J., Prospero, J., Kinne, S., Bauer, S., Boucher,
957 O., Chin, M., Dentener, F., Diehl, T., Easter, R., Fillmore, D., Ghan, S., Ginoux, P., Grini, A.,
958 Horowitz, L., Koch, D., Krol, M. C., Landing, W., Liu, X., Mahowald, N., Miller, R., Morcrette, J.-
959 J., Myhre, G., Penner, J., Perlitz, J., Stier, P., Takemura, T., and Zender, C. S.: Global dust model
960 intercomparison in AeroCom phase I, *Atmos. Chem. Phys.*, 11, 7781–7816,
961 <https://doi.org/10.5194/acp-11-7781-2011>, 2011.

962

963 Husar, R. B., Tratt, D. M., Schichtel, D. M., Falke, S. R., Li, F., Jaffe, D., Gassó, S., Gill, T.,
964 Laulainen, N. S., Lu, F., Reheis, M. C., Chun, Y., Westphal, D., Holben, B. N., Gueymard, C., McK-
965 endry, I., Kuring, N., Feldman, G. C., McClain, C., Frouin, R. J., Merrill, J., DuBois, D., Vignola, F.,
966 Murayama, T., Nickovic, S., Wilson, W. E., Sassen, K., Sugimoto, N., and Malm, W. C.: Asian dust
967 events of April 1998, *J. Geophys. Res.*, 106, 18317–18330, <https://doi.org/10.1029/2000JD900788>,
968 2001.

969

970 Ignatov, A. and Stowe, L.: Physical Basis, Premises, and SelfConsistency Checks of Aerosol
971 Retrievals from TRMM VIRS, *J. Appl. Meteor.*, 39, 2259–2277, [https://doi.org/10.1175/1520-0450\(2001\)040<2259:PBPASC>2.0.CO;2](https://doi.org/10.1175/1520-
972 0450(2001)040<2259:PBPASC>2.0.CO;2), 2000.

973
974 Indoitu, R., Kozhoridze, G., Batyrbaeva, M., Vitkovskaya, I., Orlovsky, N., Blumberg, D., Orlovsky,
975 L.: Dust emission and environmental changes in the dried bottom of the Aral Sea. *Aeolian. Res.* 17,
976 101–115, 2015, <https://doi.org/10.1016/j.aeolia.2015.02.004>.
977
978 Jickells, T. D., An, Z. S., Andersen, K. K., Baker, A. R., Bergametti, G., Brooks, N., Cao, J. J., Boyd,
979 P. W., Duce, R. A., Hunter, K. A., Kawahata, H., Kubilay, N., laRoche, J., Liss, P. S., Mahowald, N.,
980 Prospero, J. M., Ridgwell, A. J., Tegen, I., and Torres, R.: Global iron connections between desert
981 dust, ocean biogeochemistry, and climate, *Science*, 308, 67–71, 2005.
982
983 Jickells, T., Boyd, P., and Hunter, K.: Biogeochemical impacts of dust on the global carbon cycle, in:
984 *Mineral Dust*, edited by: Knippertz, P. and Stuut, J.-B. W., Springer, the Netherlands, 359– 384, 2014.
985
986 Jin, Q., Wei, J., Pu, B., Yang, Z.-L., and Parajuli, S. P.: High summertime aerosol loadings over the
987 Arabian Sea and their transport pathways. *Journal of Geophysical Research: Atmospheres*, 123, 10, 568–10,590, <https://doi.org/10.1029/2018JD028588>, 2018.
988
989
990 Johnson, M. S., Meskhidze, N., Kiliyanpilakkil, V. P., and Gassó, S.: Understanding the transport of
991 Patagonian dust and its influence on marine biological activity in the South Atlantic Ocean, *Atmos.*
992 *Chem. Phys.*, 11, 2487-2502, <https://doi.org/10.5194/acp-11-2487-2011>, 2011.
993
994 Kanakidou, M., Mihalopoulos, N., Kindap, T., Im, U., Vrekoussis, M., Gerasopoulos, E., Dermitzaki,
995 E., Unal, A., Kocak, M., Markakis, K., Melas, D., Kouvarakis, G., Youssef, A. F., Richter, A.,
996 Hatzianastassiou, N., Hilboll, A., Ebojie, F., Wittrock, F., von Savigny, C., Burrows, J. P.,
997 Ladstaetter-Weissenmayer, A., and Moubasher, H.: Megacities as hot spots of air pollution in the
998 East Mediterranean, *Atmos. Environ.*, 45, 1223–1235,
999 <https://doi.org/10.1016/j.atmosenv.2010.11.048>, 2011.
1000
1001 Kanatani, K.T., Ito, I., Al-Delaimy, W.K., Adachi, Y., Mathews, W.C., Ramsdell, J.W.: Toyama
1002 Asian Desert Dust and Asthma Study Group Members. Desert dust exposure is associated with
1003 increased risk of asthma hospitalization in children, *Am. J. Respir. Crit. Care Med.* 182 (12),
1004 1475e1481. <https://doi.org/10.1164/rccm.201002-0296OC>, 2010.
1005
1006 Kinne, S., Schulz, M., Textor, C., Guibert, S., Balkanski, Y., Bauer, S. E., Berntsen, T., Berglen, T.
1007 F., Boucher, O., Chin, M., Collins, W., Dentener, F., Diehl, T., Easter, R., Feichter, J., Fillmore, D.,

1008 Ghan, S., Ginoux, P., Gong, S., Grini, A., Hendricks, J., Herzog, M., Horowitz, L., Isaksen, I., Iversen,
1009 T., Kirkevåg, A., Kloster, S., Koch, D., Kristjansson, J. E., Krol, M., Lauer, A., Lamarque, J. F.,
1010 Lesins, G., Liu, X., Lohmann, U., Montanaro, V., Myhre, G., Penner, J., Pitari, G., Reddy, S., Seland,
1011 O., Stier, P., Takemura, T., and Tie, X.: An AeroCom initial assessment – optical properties in aerosol
1012 component modules of global models, *Atmos. Chem. Phys.*, 6, 1815–1834,
1013 <https://doi.org/10.5194/acp-6-1815-2006>, 2006.

1014

1015 Klose, M., Shao, Y., Karremann, M. K., and Fink, A.: Sahel dust zone and synoptic background,
1016 *Geophys. Res. Lett.*, 37, L09802, <https://doi.org/10.1029/2010GL042816>, 2010.

1017

1018 Knight, A. W., McTainsh, G. H., & Simpson, R. W.: Sediment loads in an Australian dust storm—
1019 Implications for present and past dust processes. *Catena*, 24(3), 195–213,
1020 [https://doi.org/10.1016/0341-8162\(95\)00026-O](https://doi.org/10.1016/0341-8162(95)00026-O), 1995.

1021

1022 Knippertz, P., Deutscher, C., Kandler, K., Müller, T., Schulz, O., and Schütz, L.: Dust mobilization
1023 due to density currents in the Atlas region: Observations from the Saharan Mineral Dust Experiment
1024 2006 field campaign, *J. Geophys. Res.-Atmos.*, 112, 1–14, <https://doi.org/10.1029/2007JD008774>,
1025 2007.

1026

1027 Knippertz, P., Evans, M., Field, P. R., Fink, A. H., Liousse, C., and Marsham, J. H.: The possible role
1028 of local air pollution in climate change in West Africa, *Nat. Clim. Chang.*, 5, 815–822,
1029 <https://doi.org/10.1038/NCLIMATE2727>, 2015.

1030

1031 Knippertz, P. and Todd, M. C.: Mineral Dust Aerosols over the Sahara: Meteorological Controls on
1032 Emission and Transport and Implications for Modeling, *Rev. Geophys.*, 50, RG1007,
1033 <https://doi.org/10.1029/2011RG000362>, 2012.

1034

1035 Koch, J. and Renno, N. O.: The role of convective plumes and vortices on the global aerosol budget,
1036 *Geophys. Res. Lett.*, 32, L18806, doi:10.1029/2005GL023420, 2005.

1037

1038 Kok, J. F., Adebiyi, A. A., Albani, S., Balkanski, Y., Checa-Garcia, R., Chin, M., Colarco, P. R.,
1039 Hamilton, D. S., Huang, Y., Ito, A., Klose, M., Leung, D. M., Li, L., Mahowald, N. M., Miller, R. L.,
1040 Obiso, V., Pérez García-Pando, C., Rocha-Lima, A., Wan, J. S., and Whicker, C. A.: Improved
1041 representation of the global dust cycle using observational constraints on dust properties and
1042 abundance, *Atmos. Chem. Phys.*, 21, 8127–8167, <https://doi.org/10.5194/acp-21-8127-2021>, 2021a.

1043

1044 Kok, J. F., Adebiyi, A. A., Albani, S., Balkanski, Y., Checa-Garcia, R., Chin, M., Colarco, P. R.,
1045 Hamilton, D. S., Huang, Y., Ito, A., Klose, M., Li, L., Mahowald, N. M., Miller, R. L., Obiso, V.,
1046 Pérez García-Pando, C., Rocha-Lima, A., and Wan, J. S.: Contribution of the world's main dust source
1047 regions to the global cycle of desert dust, *Atmos. Chem. Phys.*, 21, 8169–8193,
1048 <https://doi.org/10.5194/acp-21-8169-2021>, 2021b.

1049

1050 Koren, I., Yoram, J. K., Richard, W., Martin, C. T., Yinon, R., Martins., J. V., and Daniel, R.: The
1051 Bodélé depression: a single spot in the Sahara that provides most of the mineral dust to the Amazon
1052 forest, *Environ. Res. Lett.*, 1, 014005, <https://doi.org/10.1088/1748-9326/1/1/014005>, 2006.

1053

1054 Kosmopoulos, P.G., Kazadzis, S., El-Askary, H., Taylor, M., Gkikas, A., Proestakis, E., Kontoes, C.,
1055 El-Khayat, M.M.: Earth-Observation-Based Estimation and Forecasting of Particulate Matter Impact
1056 on Solar Energy in Egypt, *Remote Sens.*, 10, 1870, 2018.

1057

1058 Lambert, F., Kug, J.-S., Park, R. J., Mahowald, N., Winckler, G., Abe-Ouchi, A., O'ishi, R.,
1059 Takemura, T., and Lee, J.-H.: The role of mineral-dust aerosols in polar temperature amplification,
1060 *Nat. Clim. Change*, 3, 487–491, <https://doi.org/10.1038/nclimate1785>, 2013.

1061

1062 Levy, R. C., Leptoukh, G. G., Kahn, R., Zubko, V., Gopalan, A., and Remer, L. A.: A critical look at
1063 deriving monthly aerosol optical depth from satellite data, *IEEE T. Geosci. Remote*, 47, 2942–2956,
1064 <https://doi.org/10.1109/TGRS.2009.2013842>, 2009.

1065

1066 Levy, R. C., Mattoo, S., Munchak, L. A., Remer, L. A., Sayer, A. M., Patadia, F., and Hsu, N. C.:
1067 The Collection 6 MODIS aerosol products over land and ocean, *Atmos. Meas. Tech.*, 6, 2989–3034,
1068 <https://doi.org/10.5194/amt-6-2989-2013>, 2013.

1069

1070 Li, L., and Sokolik, I.: Analysis of Dust Aerosol Retrievals Using Satellite Data in Central Asia,
1071 *Atmosphere*, 9, 288, 2018.

1072

1073 Liu, D., Wang, Z., Liu, Z., Winker, D., and Trepte, C.: A height resolved global view of dust aerosols
1074 from the first year CALIPSO lidar measurements, *J. Geophys. Res.-Atmos.*, 113, D16214,
1075 <https://doi.org/10.1029/2007JD009776>, 2008.

1076

1077

1078 Logothetis, S.-A., Salamalikis, V., Gkikas, A., Kazadzis, S., Amiridis, V., and Kazantzidis, A.: 15-
1079 year variability of desert dust optical depth on global and regional scales, *Atmos. Chem. Phys.*, 21,
1080 16499–16529, <https://doi.org/10.5194/acp-21-16499-2021>, 2021.

1081

1082 Mahowald, N. M. and Luo, C.: A less dusty future?, *Geophys. Res.Lett.*, 30, 1903,
1083 <https://doi.org/10.1029/2003GL017880>, 2003.

1084

1085 Marinou, E., Amiridis, V., Binietoglou, I., Tsikerdekis, A., Solomos, S., Proestakis, E., Konsta, D.,
1086 Papagiannopoulos, N., Tsekeri, A., Vlastou, G., Zanis, P., Balis, D., Wandinger, U., and Ansmann,
1087 A.: Three-dimensional evolution of Saharan dust transport towards Europe based on a 9-year
1088 EARLINET-optimized CALIPSO dataset, *Atmos. Chem. Phys.*, 17, 5893-5919,
1089 <https://doi.org/10.5194/acp-17-5893-2017>, 2017.

1090

1091 Marticoréna, B.: Mineral Dust - A key player in the Earth system, chap. Chapter 5: Dust production
1092 mechanisms, pp. 93–120, Springer, 2014.

1093

1094 Masoom, A., Kosmopoulos, P., Bansal, A., Gkikas, A., Proestakis, E., Kazadzis, S., Amiridis, V.:
1095 Forecasting dust impact on solar energy using remote sensing and modeling techniques, *Solar Energy*,
1096 Vol. 228, 317-332, <https://doi.org/10.1016/j.solener.2021.09.033>, 2021.

1097

1098 Mazzonia, E., & Vazquez, M.: Desertification in Patagonia. In E. M. Latrubesse (Ed.), *Natural
1099 hazards and human-exacerbated disasters in Latin America*, (Vol. 13, pp. 351–377). Elsevier,
1100 [https://doi.org/https://doi.org/10.1016/S0928-2025\(08\)10017-7](https://doi.org/https://doi.org/10.1016/S0928-2025(08)10017-7), 2009.

1101

1102 McConnell, J. R., Aristarain, A. J., Banta, J. R., Edwards, P. R., and Simões, J. C.: 20th-century
1103 doubling in dust archived in an Antarctic Peninsula ice core parallels climate change and
1104 desertification in South America, *Proc. Natl. Acad. Sci. U. S. A.*, 104, 5743–5748, 2007.

1105

1106 Micklin, P.: The Aral Sea disaster, *Annu. Rev. Earth Planet. Sci.*, 35, 47–72, 2007.

1107

1108 Middleton, N. J.: Dust storms in the Middle East, *J. Arid Environ.*, 10, 83–96, 1986.

1109

1110 Middleton, H. J.: Desert dust hazards: A global review, *Aeolian Res.*, 24, 53–63, 2017.

1111

1112 Middleton, N. J. and Goudie, A. S.: Saharan dust: sources and trajectories, *T. I. Brit. Geogr.*, 26, 165–
1113 181, doi:10.1111/1475- 5661.00013, 2001.

1114

1115 Middleton, N.J., Kang, U.: Sand and dust storms: impact mitigation, *Sustainability*, 9, 1053,
1116 <https://doi.org/10.3390/su9061053>, 2017.

1117 Mitchell, R. M., Forgan, B. W., and Campbell, S. K.: The Climatology of Australian Aerosol, *Atmos.*
1118 *Chem. Phys.*, 17, 5131-5154, <https://doi.org/10.5194/acp-17-5131-2017>, 2017.

1119 Moran-Zuloaga, D., Ditas, F., Walter, D., Saturno, J., Brito, J., Carbone, S., Chi, X., Hrabě de
1120 Angelis, I., Baars, H., Godoi, R. H. M., Heese, B., Holanda, B. A., Lavrič, J. V., Martin, S. T., Ming,
1121 J., Pöhlker, M. L., Ruckteschler, N., Su, H., Wang, Y., Wang, Q., Wang, Z., Weber, B., Wolff, S.,
1122 Artaxo, P., Pöschl, U., Andreae, M. O., and Pöhlker, C.: Long-term study on coarse mode aerosols in
1123 the Amazon rain forest with the frequent intrusion of Saharan dust plumes, *Atmos. Chem. Phys.*, 18,
1124 10055-10088, <https://doi.org/10.5194/acp-18-10055-2018>, 2018.

1125

1126 Nabat, P., Somot, S., Mallet, M., Michou, M., Sevault, F., Driouech, F., Meloni, D., di Sarra, A., Di
1127 Biagio, C., Formenti, P., Sicard, M., Léon, J.-F., and Bouin, M.-N.: Dust aerosol radiative effects
1128 during summer 2012 simulated with a coupled regional aerosol–atmosphere–ocean model over the
1129 Mediterranean, *Atmos. Chem. Phys.*, 15, 3303-3326, <https://doi.org/10.5194/acp-15-3303-2015>,
1130 2015.

1131

1132 Okin, G. S., Mahowald, N., Chadwick, O. A., and Artaxo, P.: Impact of desert dust on the
1133 biogeochemistry of phosphorus in terrestrial ecosystems, *Global Biogeochem. Cy.*, 18, GB2005,
1134 <https://doi.org/10.1029/2003GB002145>, 2004.

1135

1136 O'Neill, N. T., Ignatov, A., Holben, B. N., and Eck, T. F.: The lognormal distribution as a reference
1137 for reporting aerosol optical depth statistics; Empirical tests using multi-year, multi-site AERONET
1138 Sunphotometer data, *Geophys. Res. Lett.*, 27, 3333–3336, <https://doi.org/10.1029/2000GL011581>,
1139 2000.

1140

1141 Pease, P. P., Tchakerian, V. P., and Tindale, N. W.: Aerosols over the Arabian Sea: geochemistry and
1142 source areas for Aeolian desert dust, *J. Arid Environ.*, 39, 477–496,
1143 <https://doi.org/10.1006/jare.1997.0368>, 1998.

1144

1145 Pérez, C., Nickovic, S., Pejanovic, G., Baldasano, J. M., and Özsoy, E.: Interactive dust-radiation
1146 modeling: A step to improve weather forecasts, *J. Geophys. Res.*, 111, 1–17, 2006.

1147

1148 Pérez García-Pando, C., Stanton, M. C., Diggle, P. J., Trzaska, S., Miller, R. L., Perlwitz, J. P.,
1149 Baldasano, J. M., Cuevas, E., Ceccato, P., Yaka, P., and Thomson, M. C.: Soil Dust Aerosols and
1150 Wind as Predictors of Seasonal Meningitis Incidence in Niger, *Environ. Health Perspect.*, 122, 679–
1151 686, doi:10.1289/ehp.1306640, 2014a.

1152

1153 Pérez García-Pando, C., Thomson, M.C., Stanton, M., Diggle, P., Hopson, T., Pandya, R. and Miller,
1154 R.L.: Meningitis and climate: From science to practice. *Earth Perspect.*, 1, 14, doi:10.1186/2194-
1155 6434-1-14, 2014b.

1156

1157 Peyridieu, S., Chédin, A., Capelle, V., Tsamalis, C., Pierangelo, C., Armante, R., Crevoisier, C.,
1158 Crépeau, L., Siméon, M., Ducos, F., and Scott, N. A.: Characterisation of dust aerosols in the infrared
1159 from IASI and comparison with PARASOL, MODIS, MISR, CALIOP, and AERONET observations,
1160 *Atmos. Chem. Phys.*, 13, 6065–6082, <https://doi.org/10.5194/acp-13-6065-2013>, 2013.

1161

1162 Piketh, S., Annegarn, H., and Tyson, P.: Lower tropospheric aerosol loadings over South Africa: the
1163 relative contribution of aeolian dust, industrial emissions, and biomass burning, *J. Geophys. Res.*, 104,
1164 1597–1607, 1999.

1165

1166 Prasad, A. K., Singh, S., Chauhan, S., Srivastava, M. K., Singh, R. P., and Singh, R.: Aerosol radiative
1167 forcing over the IndoGangetic plains during major dust storms, *Atmos. Environ.*, 41, 6289–6301,
1168 doi:10.1016/j.atmosenv.2007.03.060, 2007a.

1169

1170 Prasad, A. K. and Singh, R. P.: Changes in aerosol parameters during major dust storm events (2001–
1171 2005) over the Indo-Gangetic Plains using AERONET and MODIS data, *J. Geophys. Res.- Atmos.*,
1172 112, D09208, <https://doi.org/10.1029/2006JD007778>, 2007b.

1173

1174 Proestakis, E., Amiridis, V., Marinou, E., Georgoulias, A. K., Solomos, S., Kazadzis, S., Chimot, J.,
1175 Che, H., Alexandri, G., Binietoglou, I., Daskalopoulou, V., Kourtidis, K. A., de Leeuw, G., and van
1176 der A, R. J.: Nine-year spatial and temporal evolution of desert dust aerosols over South and East
1177 Asia as revealed by CALIOP, *Atmos. Chem. Phys.*, 18, 1337–1362, <https://doi.org/10.5194/acp-18-1337-2018>, 2018.

1178

1179

1180 Prospero, J. M.: Long-range transport of mineral dust in the global atmosphere: Impact of African
1181 dust on the environment of the southeastern United States, *P. Natl. Acad. Sci. USA*, 96, 3396–3403,
1182 1999.

1183

1184 Prospero, J. M., Collard, F. X., Molinie, J., and Jeannot, A.: Characterizing the annual cycle of
1185 African dust transport to the Caribbean Basin and South America and its impact on the environment
1186 and air quality, *Global Biogeochem. Cy.*, 28, 757–773, <https://doi.org/10.1002/2013gb004802>, 2014.

1187

1188 Prospero, J. M., Ginoux, P., Torres, O., Nicholson, S. E., and Gill, T. E.: Environmental
1189 characterization of global sources of atmospheric soil dust identified with the Nimbus 7 Total Ozone
1190 Mapping Spectrometer (TOMS) absorbing aerosol product, *Rev. Geophys.*, 40, 2-1–2-31, 2002.

1191

1192 Prospero, J. M. and Lamb, P. J.: African droughts and dust transport to the Caribbean: climate change
1193 implications, *Science*, 302, 1024–1027, doi:10.1126/science.1089915, 2003.

1194

1195 Querol X., Tobías, A., Pérez, N., Karanasiou, A., Amato, F., Stafoggia, M., Pérez García-Pando, C.,
1196 Ginoux, P., Forastiere, F., Gumy, S., Mudu, P., Alastuey, A.: Monitoring the impact of desert dust
1197 outbreaks for air quality for health studies, *Environ. Int.*, 130:104867, doi:
1198 10.1016/j.envint.2019.05.061. Epub 2019 Jun 14. PMID: 31207476; PMCID: PMC6686079, 2019.

1199

1200 Ramaswamy, V.P., Muraleedharan, M., Prakash Babu, C.: Mid-troposphere transport of Middle-East
1201 dust over the Arabian Sea and its effect on rainwater composition and sensitive ecosystems over India.
1202 *Scientific Reports* 7, 13676, <https://doi.org/10.1038/s41598-017-13652-1>, 2017.

1203

1204 Rajot, J. L., Formenti, P., Alfaro, S., Desboeufs, K., Chevaillier, S., Chatenet, B., Gaudichet, A.,
1205 Journet, E., Marticorena, B., Triquet, S., Maman, A., Mouget, N., and Zakou, A.: AMMA dust
1206 experiment: An overview of measurements performed during the dry season special observation
1207 period (SOP0) at the Banizoumbou (Niger) supersite, *J. Geophys. Res.*, 113, D00C14,
1208 doi:10.1029/2008jd009906, 2008.

1209 Rashki, A., Kaskaoutis, D.G., Francois, P., Kosmopoulos, P.G., Legrand, M.: Dust-storm dynamics
1210 over Sistan region, Iran: seasonality, transport characteristics and affected areas, *Aeol. Res.*, 16, 35–
1211 48, 2015.

1212 Ridley, D. A., Heald, C. L., Kok, J. F., and Zhao, C.: An observationally constrained estimate of
1213 global dust aerosol optical depth, *Atmos. Chem. Phys.*, 16, 15097–15117,
1214 <https://doi.org/10.5194/acp-16-15097-2016>, 2016.

1215

1216 Rivera Rivera, N. I., Gill, T. E., Gebhart, K. A., Hand, J. L., Bleiweiss, M. P., and Fitzgerald, R. M.:
1217 Wind modeling of Chihuahuan Desert dust outbreaks, *Atmos. Environ.*, 43(2), 347–354,
1218 doi:10.1016/j.atmosenv.2008.09.069, 2009.

1219

1220 Rodríguez, S., Cuevas, E., Prospero, J. M., Alastuey, A., Querol, X., López-Solano, J., García, M. I.,
1221 and Alonso-Pérez, S.: Modulation of Saharan dust export by the North African dipole, *Atmos. Chem.*
1222 *Phys.*, 15, 7471–7486, <https://doi.org/10.5194/acp-15-7471-2015>, 2015.

1223

1224 Rohrmann, A., Heermance, R., Kapp, P., and Cai, F. L.: Wind as the primary driver of erosion in the
1225 Qaidam Basin, China. *Earth Planet. Sci. Lett.*, 374, 1–10, <https://doi.org/10.1016/j.epsl.2013.03.011>,
1226 2013.

1227

1228 Saiko, T.A., Zonn, I.S.: Irrigation expansion and dynamics of desertification in the circum-atal region
1229 of central Asia, *Appl. Geogr.*, 20, 349–367, 2000.

1230

1231 Sayer, A. M. and Knobelispes, K. D.: How should we aggregate data? Methods accounting for the
1232 numerical distributions, with an assessment of aerosol optical depth, *Atmos. Chem. Phys.*, 19, 15023–
1233 15048, <https://doi.org/10.5194/acp-19-15023-2019>, 2019.

1234

1235 Schepanski, K., Tegen, I., Laurent, B., Heinold, B., and Macke, A.: A new Saharan dust source
1236 activation frequency map derived from MSG-SEVIRI IR channels, *Geophys. Res. Lett.*, 34, L18803,
1237 <https://doi.org/10.1029/2007GL030168>, 2007.

1238

1239 Schepanski, K., Tegen, I., Todd, M. C., Heinold, B., Bönisch, G., Laurent, B., and Macke, A.:
1240 Meteorological processes forcing Saharan dust emission inferred from MSG-SEVIRI observations of
1241 subdaily dust source activation and numerical models, *J. Geophys. Res.-Atmos.*, 114, D10201,
1242 <https://doi.org/10.1029/2008JD010325>, 2009.

1243

1244 Schepanski, K., Heinold, B., and Tegen, I.: Harmattan, Saharan heat low, and West African monsoon
1245 circulation: modulations on the Saharan dust outflow towards the North Atlantic, *Atmos. Chem.*
1246 *Phys.*, 17, 10223–10243, <https://doi.org/10.5194/acp-17-10223-2017>, 2017.

1247

1248 Shen, H., Abuduwaili, J., Samat, A., Ma, L.: A review on the research of modern aeolian dust in
1249 Central Asia, *Arab J Geosci.*, 9:625, 2016.

1250

1251 Sogacheva, L., de Leeuw, G., Rodriguez, E., Kolmonen, P., Georgoulias, A. K., Alexandri, G.,
1252 Kourtidis, K., Proestakis, E., Marinou, E., Amiridis, V., Xue, Y., and van der A, R. J.: Spatial and
1253 seasonal variations of aerosols over China from two decades of multi-satellite observations – Part 1:
1254 ATSR (1995–2011) and MODIS C6.1 (2000–2017), *Atmos. Chem. Phys.*, 18, 11389–11407,
1255 <https://doi.org/10.5194/acp-18-11389-2018>, 2018.

1256

1257 Sokolik, I. N. and Toon, O. B.: Direct radiative forcing by anthropogenic airborne mineral aerosols,
1258 *Nature*, 381, 681–683, <https://doi.org/10.1038/381681a0>, 1996.

1259

1260 Song, Q., Zhang, Z., Yu, H., Ginoux, P., and Shen, J.: Global dust optical depth climatology derived
1261 from CALIOP and MODIS aerosol retrievals on decadal timescales: regional and interannual
1262 variability, *Atmos. Chem. Phys.*, 21, 13369–13395, <https://doi.org/10.5194/acp-21-13369-2021>,
1263 2021.

1264

1265 Srivastava, A. K., Tiwari, S., Devara, P. C. S., Bisht, D. S., Srivastava, M. K., Tripathi, S. N., Goloub,
1266 P., and Holben, B. N.: Pre-monsoon aerosol characteristics over the Indo-Gangetic Basin:
1267 implications to climatic impact, *Ann. Geophys.*, 29, 789–804, <https://doi.org/10.5194/angeo-29-789-2011>, 2011.

1269 Stanelle, T., Bey, I., Raddatz, T., Reick, C., and Tegen, I.: Anthro- pogenically induced changes in
1270 twentieth century mineral dust burden and the associated impact on radiative forcing, *J. Geo- phys.*
1271 *Res.-Atmos.*, 119, 13526–13546, 2014.

1272 Stefanski, R. and Sivakumar, M. V. K.: Impacts of sand and dust storms on agriculture and potential
1273 agricultural applications of a SDSWS, *IOP Conf. Ser.: Earth Environ. Sci.*, 7, 012016, doi:
1274 10.1088/1755-1307/7/1/012016, 2009.

1275

1276 Sun, Y., Chen, H., Tada, R., Weiss, D., Lin, M., Toyoda, S., Yan, Y., and Isozaki, Y.: ESR signal
1277 intensity and crystallinity of quartz from Gobi and sandy deserts in East Asia and implication for
1278 tracing Asian dust provenance, *Geochem. Geophys. Geosy.*, 14, 2615–2627,
1279 <https://doi.org/10.1002/ggge.20162>, 2013.

1280

1281 Tanaka, T. Y. and Chiba, M.: A numerical study of the contributions of dust source regions to the
1282 global dust budget, Global Planet Change, 52, 88–104,
1283 <https://doi.org/10.1016/j.gloplacha.2006.02.002>, 2006.

1284 Tegen, I., Werner, M., Harrison, S., and Kohfeld, K.: Relative importance of climate and land use
1285 in determining present and future global soil dust emission, Geophys. Res. Lett., 31, L05105,
1286 <https://doi.org/10.1029/2003GL019216>, 2004.

1287 Tegen, I., Heinold, B., Todd, M., Helmert, J., Washington, R., and Dubovik, O.: Modelling soil dust
1288 aerosol in the Bodélé depression during the BoDEx campaign, Atmos. Chem. Phys., 6, 4345–4359,
1289 <https://doi.org/10.5194/acp-6-4345-2006>, 2006.

1290

1291 Tong, D. Q., Wang, J. X. L., Gill, T. E., Lei, H., and Wang, B. Y.: Intensified dust storm activity and
1292 Valley fever infection in the southwestern United States, Geophys. Res. Lett., 44, 4304–4312,
1293 <https://doi.org/10.1002/2017gl073524>, 2017.

1294

1295 Tyson, P.D., Garstang, M., Swap, R., Kallberg, P., Edwards, M.: An air transport climatology for
1296 subtropical southern Africa. Int. J. Climatol. 16 (3), 265–291, 1996.

1297

1298 Vickery, K. J., Eckardt, F. D., and Bryant, R. G.: A sub-basin scale dust plume source frequency
1299 inventory for southern Africa, 2005–2008, Geophys. Res. Lett., 40, 5274–5279,
1300 doi:10.1002/grl.50968, 2013.

1301

1302 Voss, K. K., and Evan, A. T.: A new satellite-based global climatology of dust aerosol optical depth.
1303 Journal of Applied Meteorology and Climatology, doi:10.1175/jamc-d-19-0194.1, 2020.

1304

1305 Wagener, T., Guieu, C., Losno, R., Bonnet, S., and Mahowald, N.: Revisiting atmospheric dust export
1306 to the Southern Hemisphere ocean: Biogeochemical implications, Glob. Biogeochem. Cy., 22,
1307 GB2006, <https://doi.org/10.1029/2007gb002984>, 2008.

1308

1309 Washington, R., Todd, M., Middleton, N. J., and Goudie, A. S.: Dust-storm source areas determined
1310 by the total ozone monitoring spectrometer and surface observations, Ann. Assoc. Am. Geogr., 93,
1311 297–313, <https://doi.org/10.1111/1467-8306.9302003>, 2003.

1312

1313 Washington, R. and Todd, M. C.: Atmospheric controls on mineral dust emission from the Bodélé
1314 depression, Chad: The role of the low level jet, *Geophys. Res. Lett.*, 32, L17701,
1315 <https://doi.org/10.1029/2005GL023597>, 2005.

1316

1317 Washington, R., Bouet, C., Cautenet, G., Mackenzie, E., Ashpole, I., Engelstaedter, S., Lizcano, G.,
1318 Henderson, G. M., Schepanski, K., and Tegen, I.: Dust as a tipping element: the Bodélé Depression,
1319 Chad, *P. Natl. Acad. Sci. USA*, 106, 20564–20571, doi:10.1073/pnas.0711850106, 2009.

1320

1321 Weinzierl, B., Sauer, D., Minikin, A., Reitebuch, O., Dahlkotter, F., Mayer, B., Emde, C., Tegen, I.,
1322 Gasteiger, J., Petzold, A., Veira, A., Kueppers, U., and Schumann, U.: On the visibility of airborne
1323 volcanic ash and mineral dust from the pilot's perspective in flight, *Phys Chem Earth*, 45-46, 87-102,
1324 10.1016/j.pce.2012.04.003, 2012.

1325

1326 Winker, D. M., Vaughan, M. A., Omar, A., Hu, Y., Powell, K. A., Liu, Z., Hunt, W. H. and Young,
1327 S. A.: Overview of the CALIPSO Mission and CALIOP Data Processing Algorithms, *J. Atmos.*
1328 *Oceanic Technol.*, 26(11), 2310–2323, doi:10.1175/2009JTECHA1281.1, 2009.

1329

1330 Yu, H. B., Chin, M., Winker, D. M., Omar, A. H., Liu, Z. Y., Kittaka, C., and Diehl, T.: Global view
1331 of aerosol vertical distributions from CALIPSO lidar measurements and GOCART simulations:
1332 Regional and seasonal variations, *J. Geophys. Res.-Atmos.*, 115, D00H30,
1333 <https://doi.org/10.1029/2009jd013364>, 2010.

1334

1335 Yu, H. B., Chin, M., Yuan, T. L., Bian, H. S., Remer, L. A., Prospero, J. M., Omar, A., Winker, D.,
1336 Yang, Y. K., Zhang, Y., Zhang, Z. B., and Zhao, C.: The fertilizing role of African dust in the Amazon
1337 rainforest: A first multiyear assessment based on data from Cloud-Aerosol Lidar and Infrared
1338 Pathfinder Satellite Observations, *Geophys. Res. Lett.*, 42, 1984–1991,
1339 <https://doi.org/10.1002/2015gl063040>, 2015.

1340

1341 Yu, H., Remer, L. A., Chin, M., Bian, H., Kleidman, R. G., and Diehl, T.: A satellite-based assessment
1342 of transpacific transport of pollution aerosol, *J. Geophys. Res.-Atmos.*, 113, D14S12,
1343 <https://doi.org/10.1029/2007JD009349>, 2008.

1344

1345 Yu, Y., Kalashnikova, O. V., Garay, M. J., and Notaro, M.: Climatology of Asian dust activation and
1346 transport potential based on MISR satellite observations and trajectory analysis, *Atmos. Chem. Phys.*,
1347 19, 363-378, <https://doi.org/10.5194/acp-19-363-2019>, 2019.

1348

1349 Yu, Y., Notaro, M., Kalashnikowa, O., Garay, M.: Climatology of summer Shamal wind in the
1350 Middle East, *J. Geophys. Res.-Atmos.* 121 (1), 289–305, 2016.

1351

1352 Yu, Y., Notaro, M., Liu, Z., Kalashnikova, O., Alkolibi, F., Fadda, E., and Bakhrjy, F.: Assessing
1353 temporal and spatial variations in atmospheric dust over Saudi Arabia through satellite, radiometric,
1354 and station data, *J. Geophys. Res.-Atmos.*, 118, 13253– 13264,
1355 <https://doi.org/10.1002/2013JD020677>, 2013.

1356

1357 Yu, Y., Kalashnikova, O. V., Garay, M. J., Lee, H., Choi, M., Okin, G. S., Yorks, J. E., Campbell, J.
1358 R., and Marquis, J.: A global analysis of diurnal variability in dust and dust mixture using CATS
1359 observations, *Atmos. Chem. Phys.*, 21, 1427–1447, <https://doi.org/10.5194/acp-21-1427-2021>, 2021.

1360

1361 Xi, X. and Sokolik, I. N.: Seasonal dynamics of threshold friction velocity and dust emission in
1362 Central Asia, *J. Geophys. Res. Atmos.*, 120(4), 1536–1564, doi:10.1002/2014JD022471, 2015.

1363

1364 Zender, C. S., Huisheng, B., and Newman, D.: Mineral Dust Entrainment and Deposition (DEAD)
1365 model: Description and 1990s dust climatology, *J. Geophys. Res.*, 108, 4416,
1366 <https://doi.org/10.1029/2002JD002775>, 2003.

1367

1368

1369

1370

1371

1372

1373

1374

1375

1376

1377

1378

1379

1380

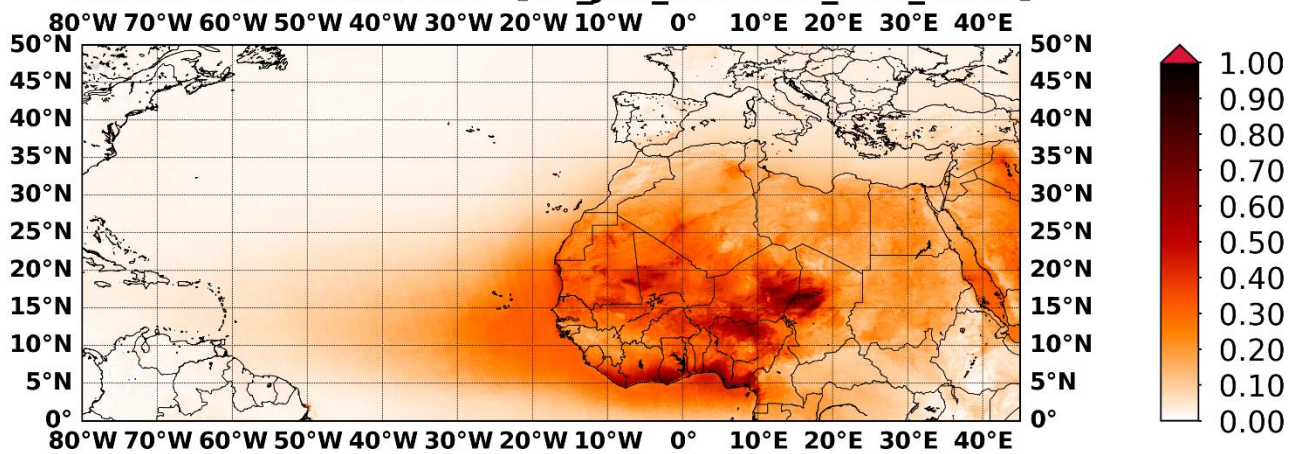
1381

1382 **Table 1:** Annual and seasonal DOD averages, representative for the period 2003-2017, along with the associated
 1383 uncertainty. The first three rows refer to the whole globe (GLB), the global land (GLB-land) and global ocean (GLB-
 1384 ocean). In the fourth and fifth line are given the results for N. Hemisphere (NHE) and S. Hemisphere (SHE) DODs
 1385 whereas in the rest 17 entries the corresponding results for selected subregions (denoted with colored rectangles in Fig. 7
 1386 in Gkikas et al. (2021)) are given.

REGION	ANNUAL	DJF	MAM	JJA	SON
GLB	0.032 ± 0.003	0.025 ± 0.004	0.043 ± 0.005	0.040 ± 0.005	0.022 ± 0.004
GLB-land	0.070 ± 0.005	0.063 ± 0.008	0.104 ± 0.011	0.083 ± 0.010	0.049 ± 0.007
GLA-ocean	0.019 ± 0.002	0.015 ± 0.003	0.026 ± 0.003	0.023 ± 0.003	0.012 ± 0.003
NHE	0.056 ± 0.004	0.043 ± 0.005	0.085 ± 0.009	0.071 ± 0.008	0.036 ± 0.005
SHE	0.008 ± 0.001	0.010 ± 0.003	0.008 ± 0.002	0.006 ± 0.002	0.008 ± 0.003
BOD	0.533 ± 0.009	0.483 ± 0.018	0.614 ± 0.020	0.603 ± 0.017	0.451 ± 0.013
GOB	0.092 ± 0.007	0.074 ± 0.010	0.189 ± 0.023	0.078 ± 0.010	0.056 ± 0.005
CAS	0.126 ± 0.007	0.084 ± 0.012	0.158 ± 0.016	0.144 ± 0.011	0.100 ± 0.007
NME	0.227 ± 0.006	0.120 ± 0.009	0.319 ± 0.016	0.271 ± 0.011	0.186 ± 0.009
SUS	0.018 ± 0.001	0.009 ± 0.002	0.033 ± 0.005	0.021 ± 0.003	0.010 ± 0.001
TAK	0.246 ± 0.020	0.114 ± 0.015	0.504 ± 0.047	0.259 ± 0.030	0.130 ± 0.018
THA	0.198 ± 0.007	0.086 ± 0.006	0.291 ± 0.013	0.424 ± 0.033	0.109 ± 0.006
WSA	0.302 ± 0.006	0.199 ± 0.008	0.362 ± 0.015	0.418 ± 0.016	0.237 ± 0.009
EAS	0.077 ± 0.005	0.072 ± 0.014	0.130 ± 0.012	0.056 ± 0.010	0.048 ± 0.006
ENP	0.020 ± 0.002	0.011 ± 0.002	0.047 ± 0.005	0.017 ± 0.004	0.013 ± 0.002
ETA	0.146 ± 0.007	0.109 ± 0.011	0.169 ± 0.015	0.202 ± 0.015	0.093 ± 0.009
GOG	0.309 ± 0.021	0.417 ± 0.032	0.416 ± 0.066	0.064 ± 0.021	0.100 ± 0.022
MED	0.081 ± 0.003	0.052 ± 0.008	0.106 ± 0.009	0.096 ± 0.006	0.066 ± 0.005
SME	0.250 ± 0.008	0.154 ± 0.009	0.318 ± 0.016	0.394 ± 0.020	0.166 ± 0.008
SSA	0.326 ± 0.013	0.309 ± 0.015	0.494 ± 0.041	0.241 ± 0.054	0.199 ± 0.020
WNP	0.028 ± 0.002	0.017 ± 0.003	0.064 ± 0.008	0.023 ± 0.006	0.018 ± 0.002
WTA	0.035 ± 0.003	0.006 ± 0.002	0.035 ± 0.005	0.090 ± 0.009	0.017 ± 0.004

1387
 1388
 1389
 1390
 1391
 1392
 1393

MIDAS-DOD ANNUAL [01_Jan_2003-31_Dec_2017]

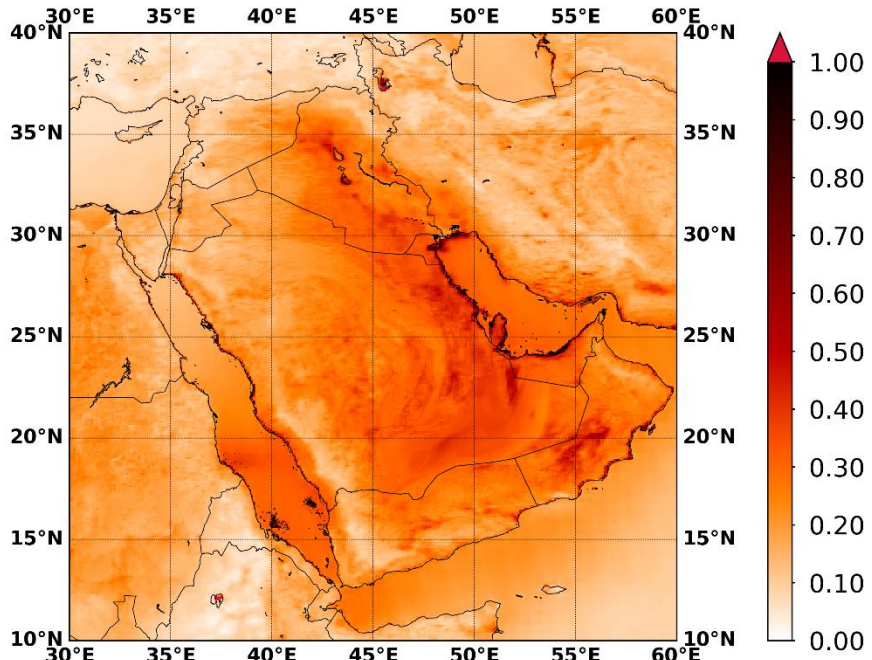


1394

1395 **Figure 1:** Geographical distribution of the MIDAS annual DOD at 550nm, representative for the period 1 January 2003
1396 – 31 December 2017, over North Africa, the Tropical Atlantic Ocean and the broader Mediterranean basin.

1397

MIDAS-DOD ANNUAL [01_Jan_2003-31_Dec_2017]

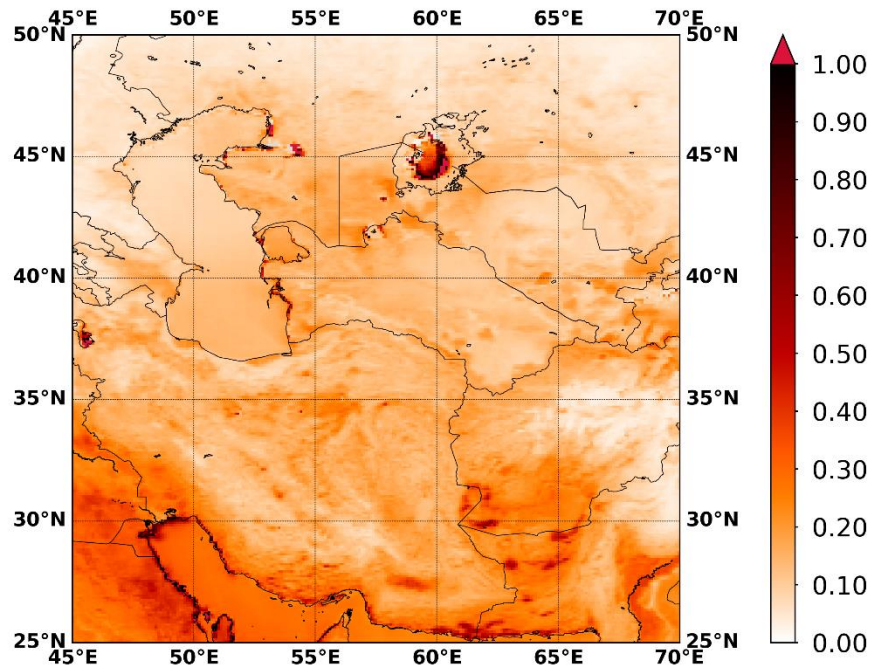


1398

1399 **Figure 2:** As in Figure 1 but for the broader area of the Middle East.

1400

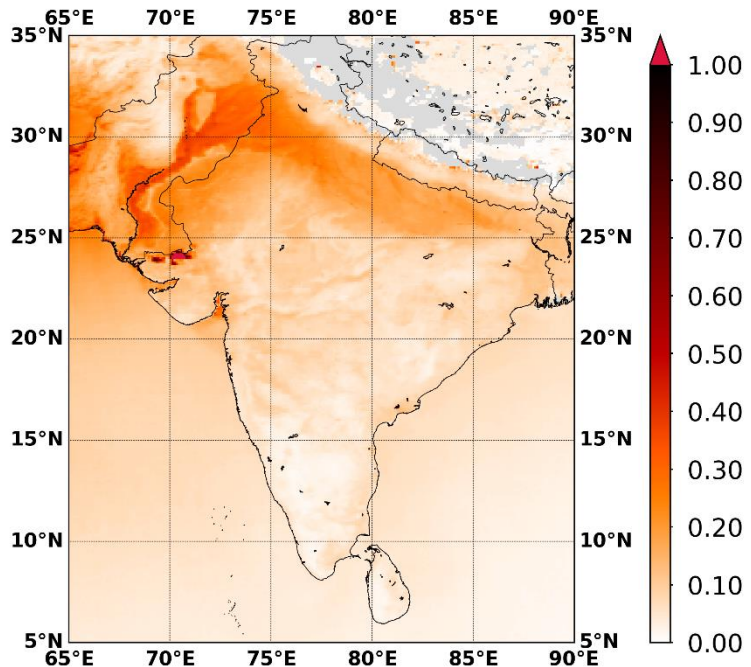
MIDAS-DOD ANNUAL [01_Jan_2003-31_Dec_2017]



1401
1402
1403

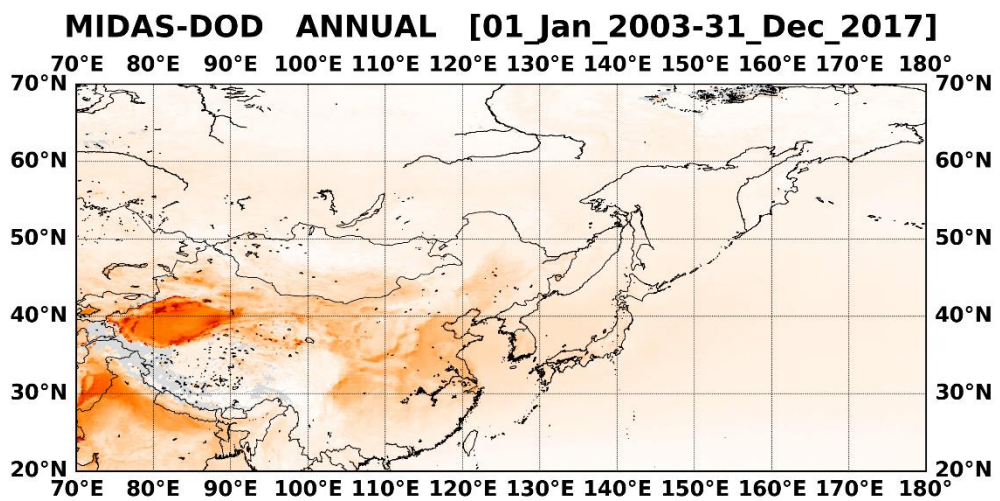
Figure 3: As in Figure 1 but for central and southwestern Asia.

MIDAS-DOD ANNUAL [01_Jan_2003-31_Dec_2017]



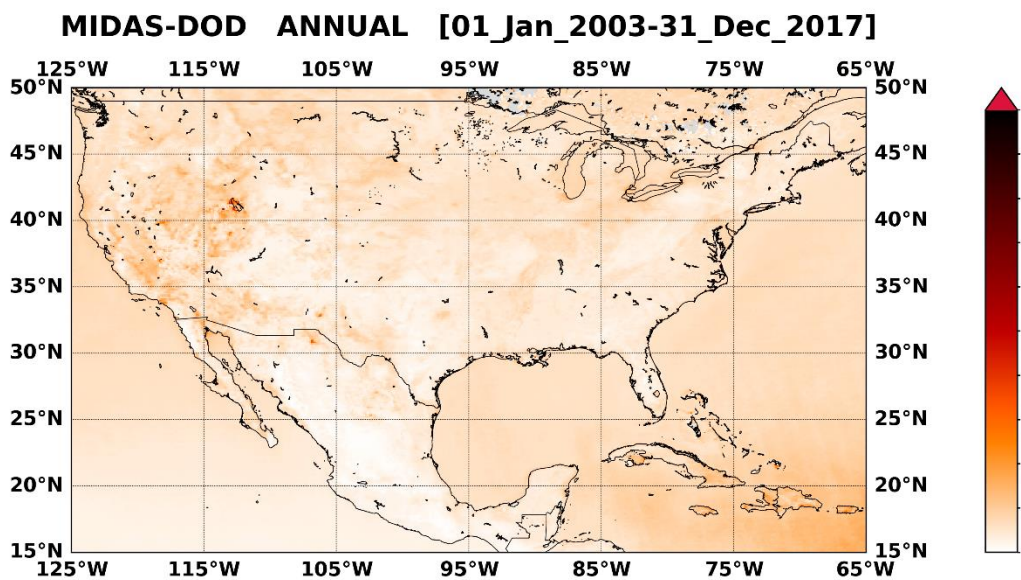
1404
1405
1406

Figure 4: As in Figure 1 but for the Indian subcontinent.



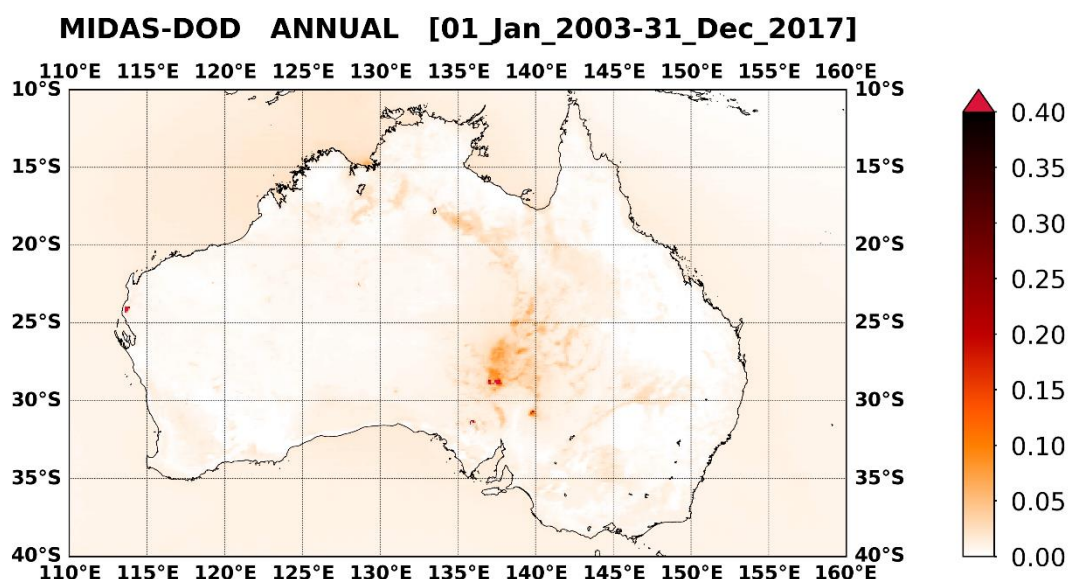
1407
1408
1409

Figure 5: As in Figure 1 but for East Asia and the North Pacific Ocean.



1410
1411
1412

Figure 6: As in Figure 1 but for North America.



1413
1414
1415

Figure 7: As in Figure 1 but for Australia.

MIDAS-DOD ANNUAL [01_Jan_2003-31_Dec_2017]

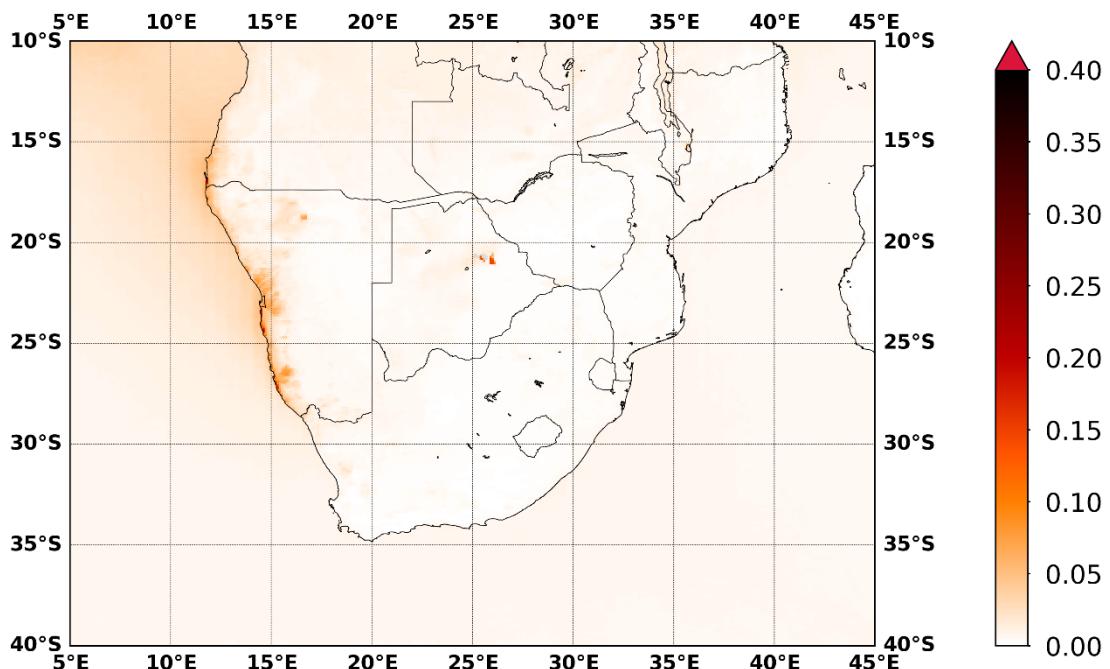


Figure 8: As in Figure 1 but for Southern Africa.

MIDAS-DOD ANNUAL [01_Jan_2003-31_Dec_2017]

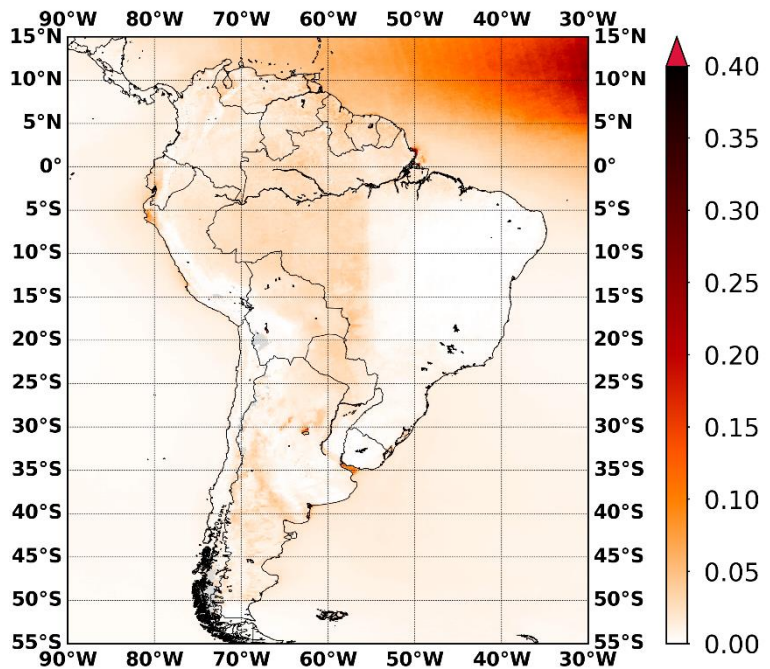
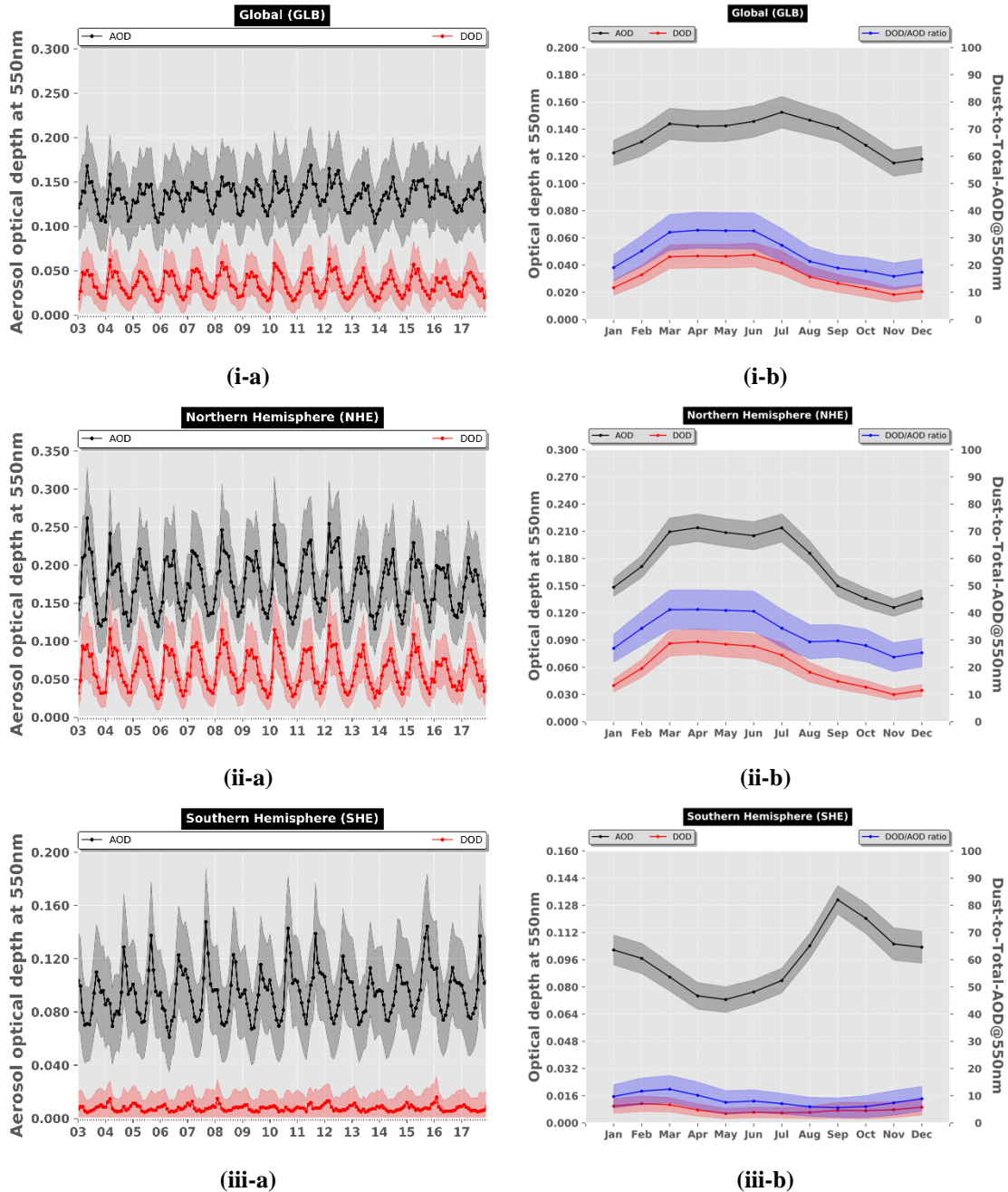


Figure 9: As in Figure 1 but for South America.



1431 **Figure 10:** Inter-annual (-a) and intra-annual (-b) variability, representative for the period 2007 – 2016, of monthly
1432 MODIS AOD_{550nm} (black curve) and DOD_{550nm} (red curve) regionally averaged for: (i) the whole globe (GLB), (ii) the
1433 Northern Hemisphere (NHE) and (iii) the Southern Hemisphere (SHE). The blue curves in the intra-annual plots depict
1434 the dust-to-total AOD_{550nm} ratio (expressed in percentage; right y-axis). The shaded areas correspond to the total
1435 uncertainty.

1436

1437

1438

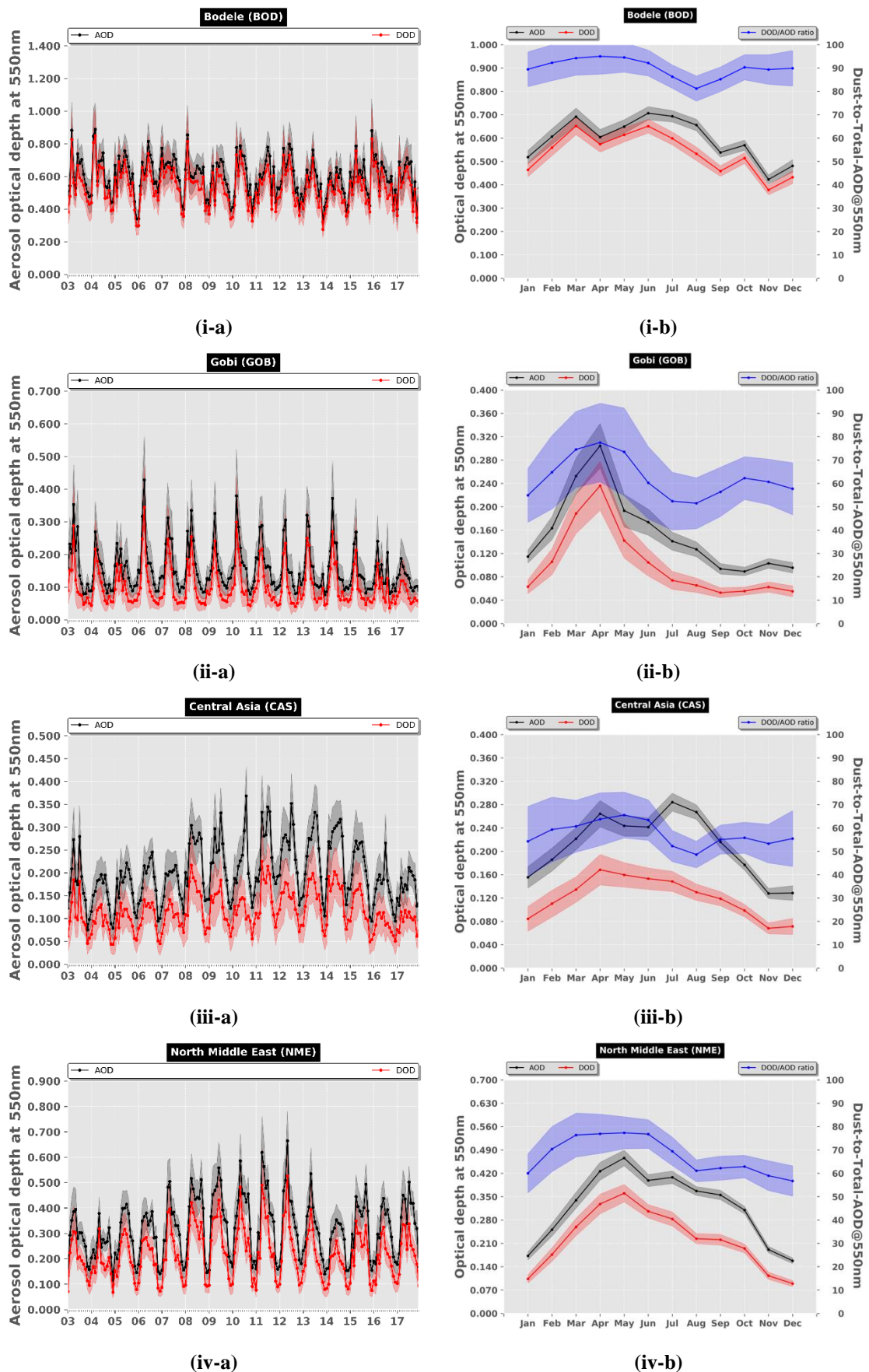
1439

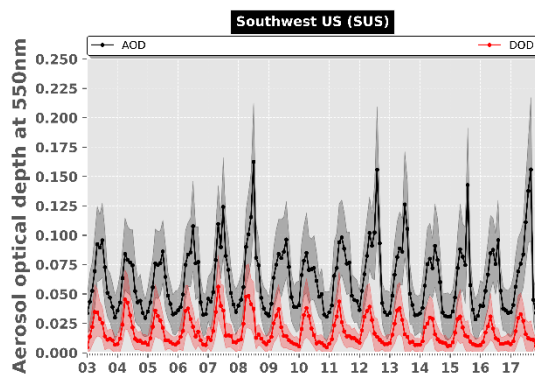
1440

1441

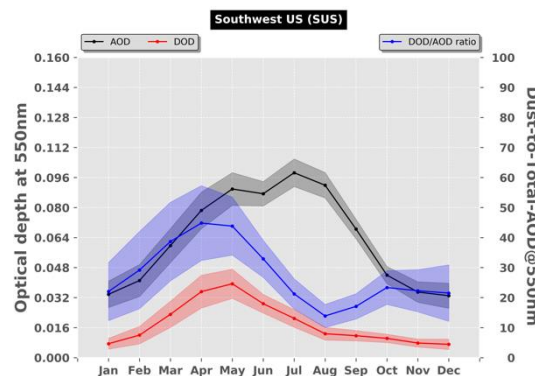
1442

1443

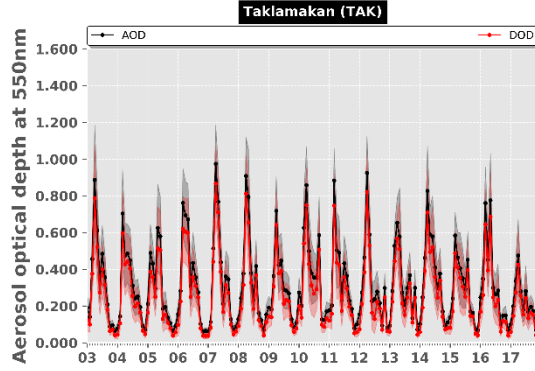




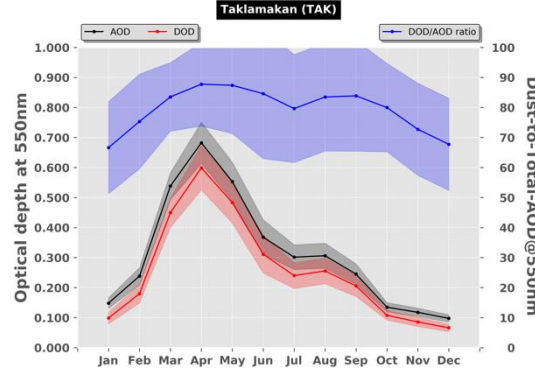
(v-a)



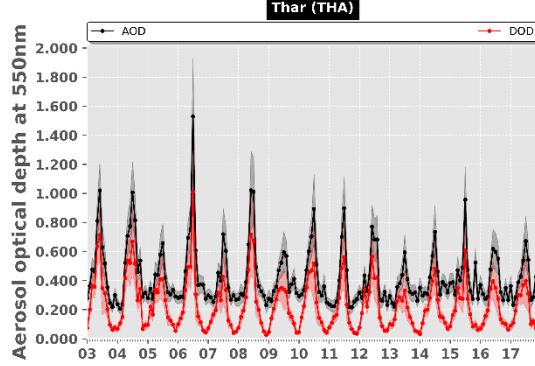
(v-b)



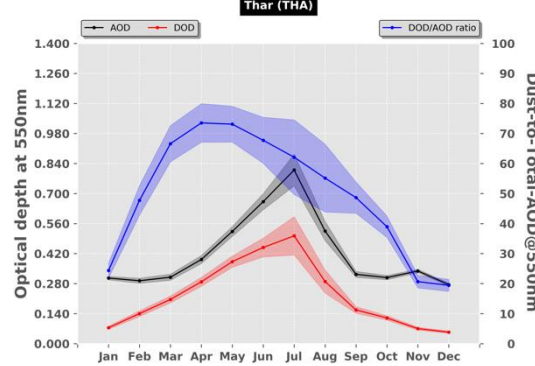
(vi-a)



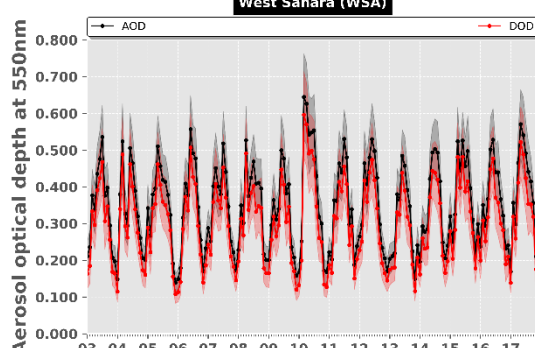
(vi-b)



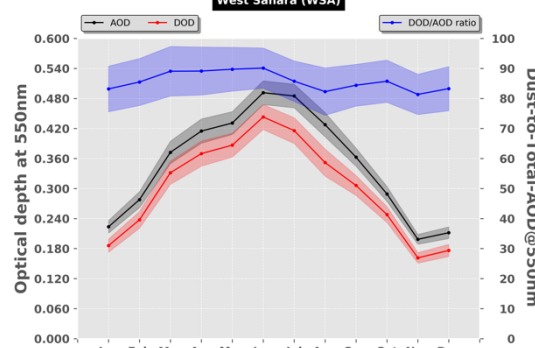
(vii-a)



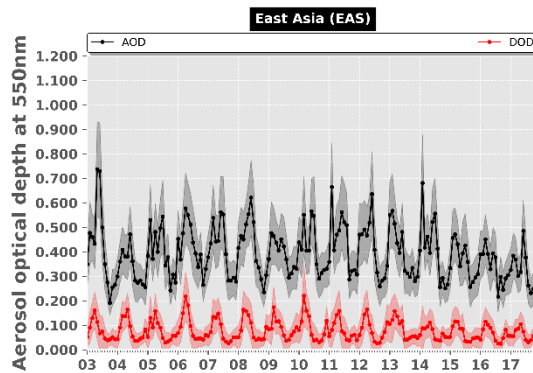
(vii-b)



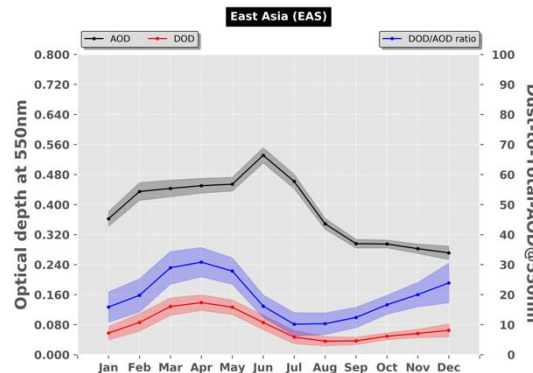
(viii-a)



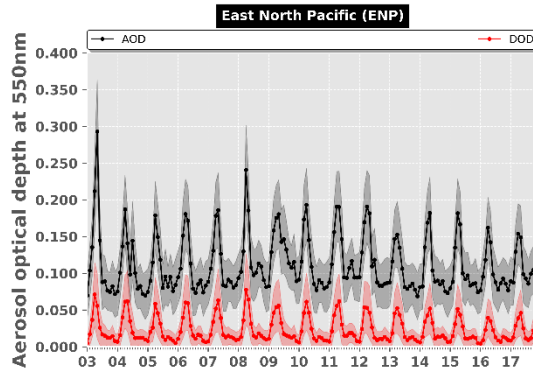
(viii-b)



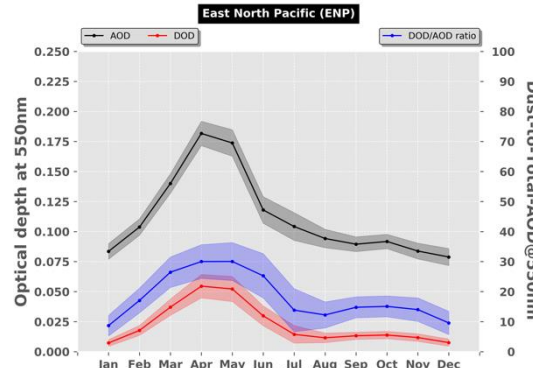
(ix-a)



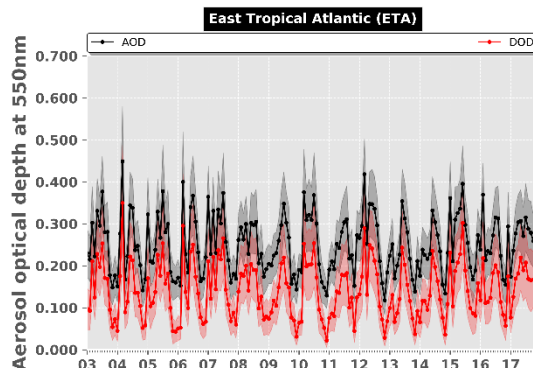
(ix-b)



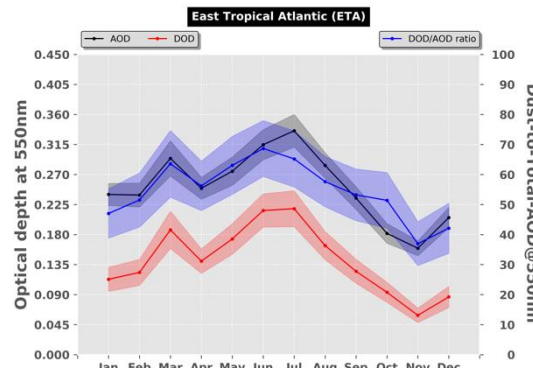
(x-a)



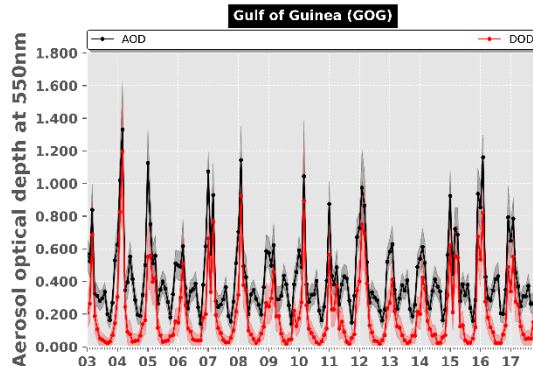
(x-b)



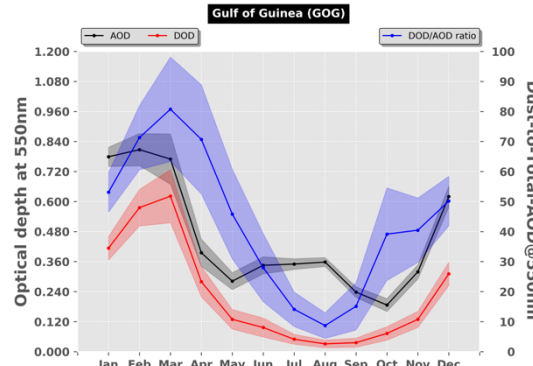
(xi-a)



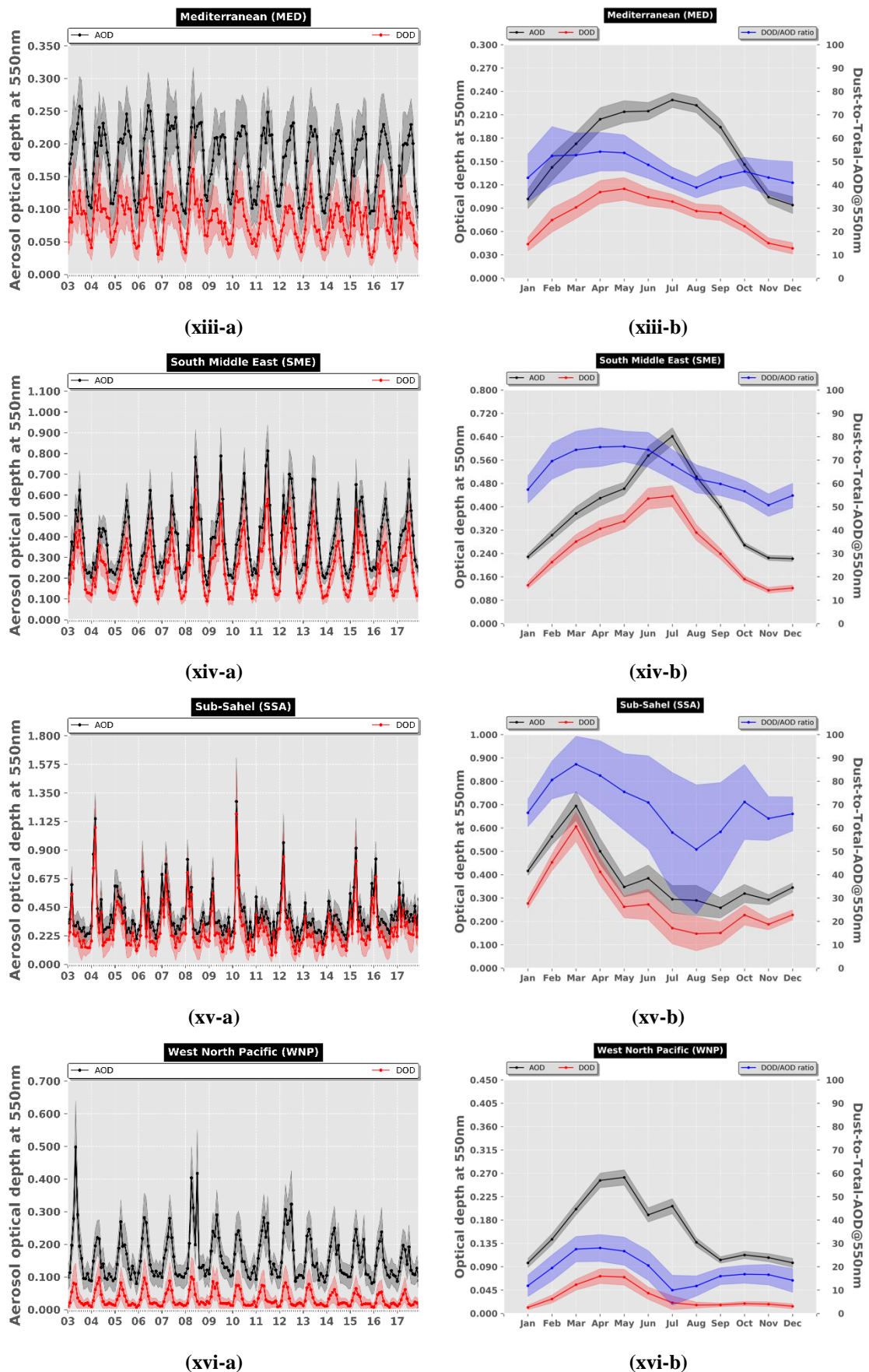
(xi-b)

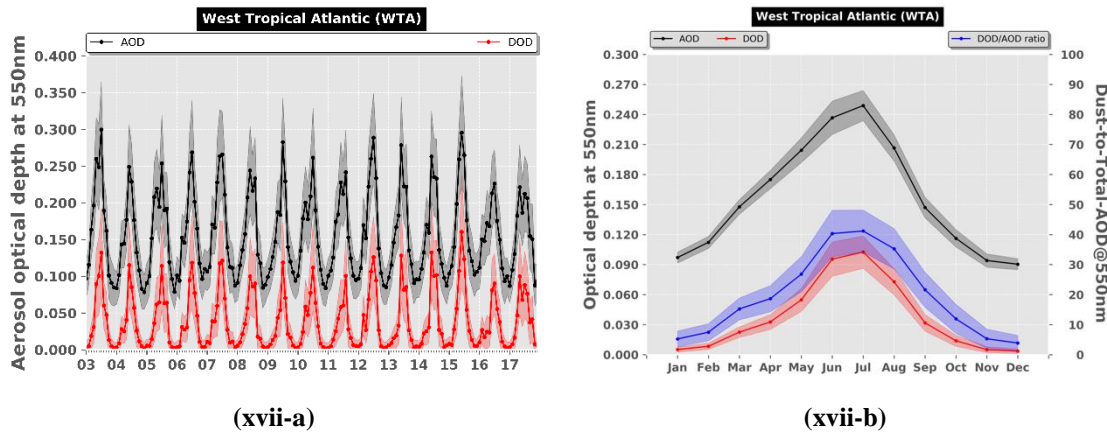


(xii-a)



(xii-b)





1444 **Figure 11:** Inter-annual (-a) and intra-annual (-b) variability, representative for the period 2003 – 2017, of monthly
1445 MODIS AOD_{550nm} (black curve) and DOD_{550nm} (red curve) regionally averaged for: (i) Bodélé Depression (BOD), (ii)
1446 Gobi Desert (GOB), (iii) Central Asia (CAS), (iv) North Middle East (NME), (v) southwest United States (SUS), (vi)
1447 Taklamakan Desert (TAK), (vii) Thar Desert (THA), (viii) West Sahara (WSA), (ix) East Asia (EAS), (x) East North
1448 Pacific (ENP), (xi) East Tropical Atlantic (ETA), (xii) Gulf of Guinea (GOG), (xiii) Mediterranean (MED), (xiv) South
1449 Middle East (SME), (xv) Sub-Sahel (SSA), (xvi) West North Pacific (WNP) and (xvii) West Tropical Atlantic (WTA).
1450 The shaded areas in the inter and intra-annual plots correspond to the total uncertainty. The blue curves in the intra-annual
1451 plots represent the percentage contribution of dust optical depth (DOD) to the aerosol optical depth (AOD).

1452

1453

1454

1455

1456

1457

1458

1459

1460

1461

1462

1463

1464

1465

1466

1467

1468

1469

1470

1471

1472

1473

1474

1475

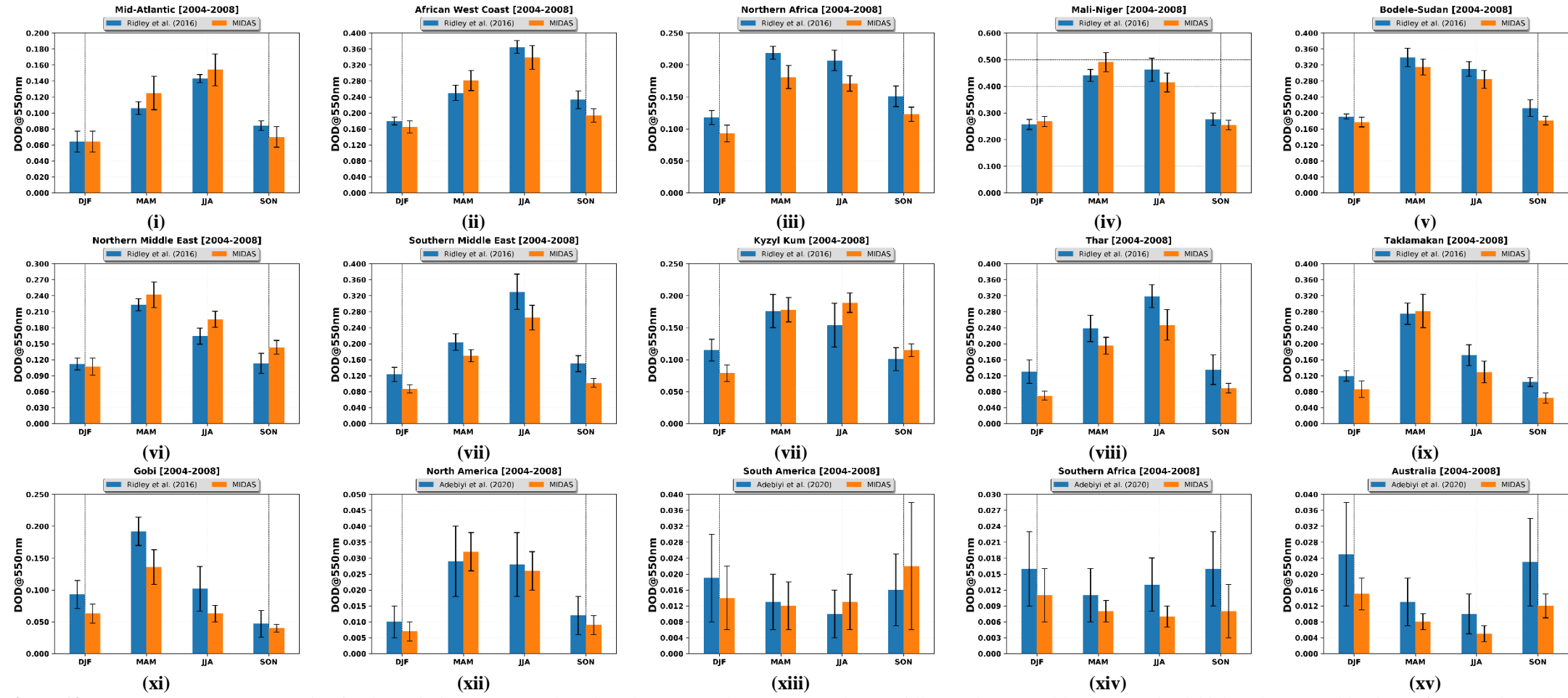


Figure 12: Seasonal DODs, representative for the period 2004 – 2008, based on the MIDAS dataset (orange bars), Ridley et al. (2016) (blue bars) and Adebiyi et al. (2020) (blue bars), for 15 regions (their names are given at the top of each plot) defined in Kok et al. (2021a) (see Table 2). The error bars represent the estimated uncertainties. From i to xi, the blue bars correspond to the Ridley et al. (2016) results whereas for the remaining regions MIDAS DODs are compared against the corresponding levels obtained by Adebiyi et al. (2020).